Remote Sensing of Environment 270 (2022) 112861

Contents lists available at ScienceDirect

Remote Sensing of Environment

journal homepage: www.elsevier.com/locate/rse

A neural network-based method for satellite-based mapping of sediment-laden sea ice in the Arctic

Hisatomo Waga [a,b,*], Hajo Eicken [a,c], Bonnie Light [d], Yasushi Fukamachi [b]

[a] International Arctic Research Center, University of Alaska Fairbanks, 2160 Koyukuk Drive, Fairbanks, AK 99775, USA
[b] Arctic Research Center, Hokkaido University, N21 W11, Kita-ku, Sapporo, Hokkaido 001-0021, Japan
[c] Visiting Faculty, Arctic Research Center, Hokkaido University, N21 W11, Kita-ku, Sapporo, Hokkaido 001-0021, Japan
[d] Polar Science Center, Applied Physics Laboratory, University of Washington, 1013 NE 40th Street, Seattle, Washington 98106, USA

ARTICLE INFO

Editor: Menghua Wang

Keywords:
Arctic
Sea ice
Machine learning
Remote sensing

ABSTRACT

Sediment-laden sea ice is a ubiquitous phenomenon in the Arctic Ocean and its marginal seas. This study presents a satellite-based approach at quantifying the distribution of sediment-laden ice that allows for more extensive observations in both time and space to monitor spatiotemporal variations in sediment-laden ice. A structural-optical model coupled with a four-stream multilayer discrete ordinates method radiative transfer model was used to examine surface spectral albedo for four surface types: clean ice, sediment-laden ice with 15 different sediment loadings from 25 to 1000 g m^{-3}, ponded ice, and ice-free open water. Based on the fact that the spectral characteristics of sediment-laden ice differ from those other surface types, fractions of sediment-laden ice were estimated from the remotely-sensed surface reflectance by a spectral unmixing algorithm using a least square method. Sensitivity analyses demonstrated that a combination of sediment loads of 50 and 500 g m^{-3} effectively represents the areal fraction of sediment-laden ice with a wide range of sediment loads. The estimated fractions of each surface type and corresponding remotely-sensed surface reflectances were used to train an artificial neural network to speed up processing relative to the least squares method. Comparing the fractions of sediment-laden ice derived from these two approaches yielded good agreements for areal fractions of sediment-laden ice, highlighting the superior performance of the neural network for processing large datasets. Although our approach contains potential uncertainties associated with methodological limitations, spatiotemporal variations in sediment-laden ice exhibited reasonable agreement with spatial patterns and seasonal variations reported in the literature on in situ observations of sediment-laden ice. Systematic satellite-based monitoring of sediment-laden ice distribution can provide extensive, sustained, and cost-effective observations to foster our understanding of the role of sediment-laden ice in a wide variety of research fields including sediment transport and biogeochemical cycling.

1. Introduction

Sediment-laden sea ice (Fig. 1), also referred to as "dirty" sea ice, is a ubiquitous feature in the Arctic Ocean and its marginal seas (Barber et al., 2021; Darby et al., 2011; Eicken et al., 2000, 2005). Indeed, sediment-laden ice covers a substantial fraction of the total ice coverage, with a maximum of 40–60% in the Chukchi Sea (Tucker et al., 1999). Sediment entrainment into sea ice is likely caused by a direct interaction between frazil ice and resuspended sediments (Ito et al., 2015, 2019). Sea-ice transport of sediments plays an important role in redistribution and dispersal of suspended pollutants (Pfirman et al., 1995). Sediments incorporated into sea ice are an important source of iron and nutrients released during ice melt and support phytoplankton growth (Kanna et al., 2014; Nomura et al., 2010). At the same time, sediment entrainment into sea ice is a major constraint on in-ice and under-ice primary production (Gradinger et al., 2009). Considering these key roles and recent shifts in the Arctic ice regimes (reduced summer minimum ice extent, ice thinning, reduction in multi-year ice extent, altered drift paths and mid-winter landfast ice break-out events) that have likely increased the amount of sediment-laden ice in the Arctic (Eicken et al., 2005), it is important to establish a method for monitoring large-scale variations in sediment-laden ice.

Satellite remote sensing is an effective technique for large-scale observations of Arctic sea ice because sea-ice condition vary substantially

* Corresponding author at: International Arctic Research Center, University of Alaska Fairbanks, 2160 Koyukuk Drive, Fairbanks, AK 99775, USA
E-mail addresses: hwaga@alaska.edu (H. Waga), heicken@alaska.edu (H. Eicken), bonlight@uw.edu (B. Light), yasuf@arc.hokudai.ac.jp (Y. Fukamachi).

https://doi.org/10.1016/j.rse.2021.112861
Received 26 May 2021; Received in revised form 11 December 2021; Accepted 20 December 2021
Available online 28 December 2021

within a short time span due to changes in ice variables such as snowfall, snow/ice melting, ponding, and meltwater drainage (Eicken et al., 2002; Perovich et al., 2007, 2017). Spaceborne optical sensors such as the Advanced Visible High Resolution Radiometer (AVHRR) and the Moderate Resolution Imaging Spectroradiometer (MODIS), as well as spaceborne passive microwave sensors such as the Advanced Microwave Scanning Radiometer – Earth Observing System (AMSR-E) and the Special Sensor Microwave/Imager (SSM/I), have provided essential data for different variables such as sea-ice extent, concentration, and surface reflectance over the decades. Huck et al. (2007) developed an approach to map the distribution of sediment-laden ice in the Arctic based on sea-ice albedo at two bands (visible and near-infrared) observed by AVHRR. Eicken et al. (2000) combined in situ sampling with remotely-sensed data from the Satellite Pour l'Observation de la Terre (SPOT) and AVHRR to determine sediment loads in sea ice in the Siberian Arctic. Furthermore, Zhang et al. (2015) developed an inversion algorithm based on the Classification and Regression Tree (CART) to detect sea ice in sediment-laden water using MODIS imagery in the Bohai Bay. In recent years, Barber et al. (2021) detected distribution of five surface types including sediment-laden ice using a supervised classification method based on surface reflectance of surface types at three MODIS bands. Overall, satellite-based methods for detecting sediment-laden ice have often been developed in the various regions. However, sea ice is a complex mosaic of a broader range of surface types, such as bare ice, snow, melt ponds, leads and open ocean (Perovich et al., 2002; Perovich and Polashenski, 2012), and the resulting existence of mixed surface types within a grid cell has been the main obstacle for satellite image interpretation and quantification (Zhang et al., 2011).

Meanwhile, Tschudi et al. (2008) proposed a spectral unmixing algorithm for monitoring the spatial distribution of ponded ice using MODIS surface reflectance data. Spectral unmixing is the process by which the measured spectrum of a pixel is decomposed into a collection of constituent spectra, or endmembers, and a set of corresponding fractions, or abundances, indicating the proportion of each endmember present in the pixel (Shah and Varshney, 2004). This approach utilized differences in the spectral signatures of surface types, including ponded ice, white ice, snow-covered ice, and open water, and successfully estimated fractional coverages of ponded ice from space. As the spectral signatures of sediment-laden ice differ substantially from other surface types, the distribution of sediment-laden ice can be extracted from remotely-sensed sea-ice reflectance data as well. The key feature of this approach is the exploitation of the frequent temporal coverage and comprehensive spectral information available from satellites to provide ice-surface type information at sampling frequencies and over areas sufficiently large to be useful for climate studies and model evaluation (Tschudi et al., 2008).

Here, we present a method for detecting the distribution of sediment-laden ice using satellite-derived surface reflectance, based on an artificial neural network (ANN). ANNs are adaptive systems that consist of several neurons organized in hierarchical layers in which each neuron of a layer is fully interconnected to all neurons in the adjacent two layers through weighted paths. One of the main advantages of ANNs is their ability to learn relationships in data from training data without predefined or explicated equations (Marzban, 2009). Furthermore, once trained, ANNs are powerful tools for fast and efficient processing of large datasets such as satellite data (Paul and Huntemann, 2021). ANNs have been widely used for biogeochemical (Fourrier et al., 2020; Li et al., 2020a; Sauzède et al., 2016), geophysical (Boulze et al., 2020; Chen et al., 2018; Paul and Huntemann, 2021), and ecological applications (Hu et al., 2018; Syariz et al., 2020). In fact, Rösel et al. (2012) successfully developed an ANN-based method to derive melt pond fractions for Arctic sea-ice surfaces.

Given the potential importance of satellite-based mapping of sediment-laden ice, this study proposes a new approach to monitor sediment-laden ice from space, and explore spatiotemporal variations in sediment-laden ice at the pan-Arctic scale for the first time. The paper is organized as follows. First, spectral signatures of sediment-laden ice and other surface types are simulated using a radiative transfer model; next,

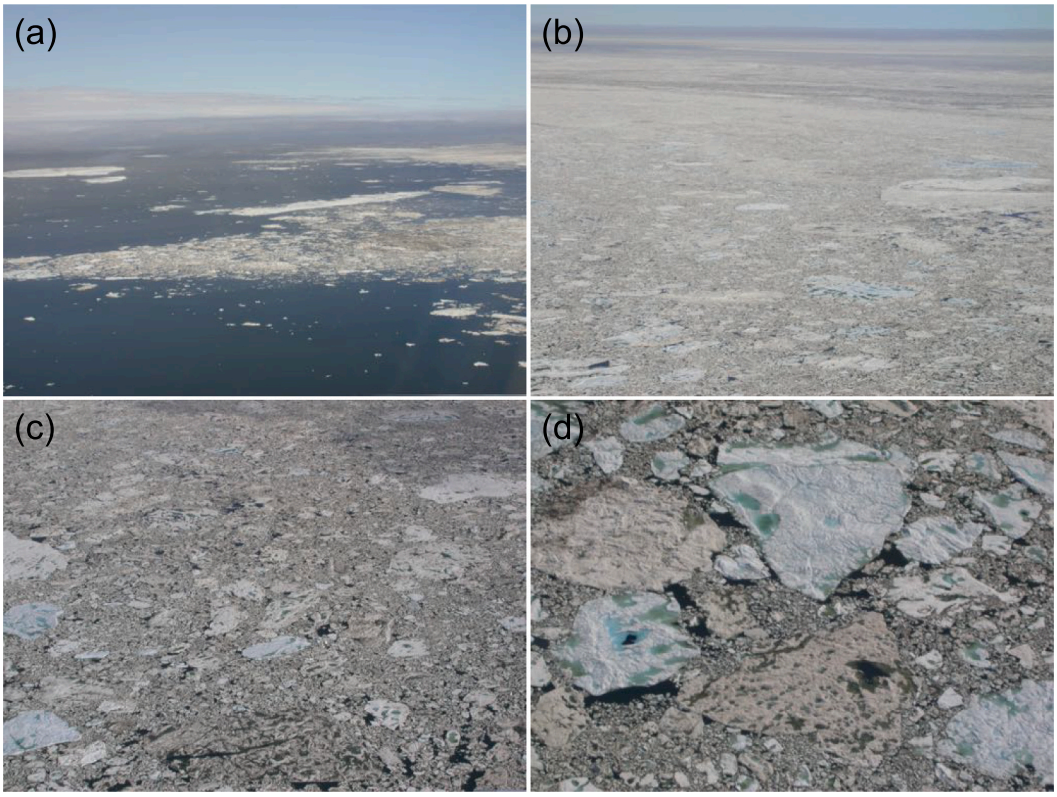

Fig. 1. Photographs of sediment-laden ice taken near Point Barrow on July 30, 2006 (see Fig. 2).

based on the spectral signature of each surface type, fractions of each surface type are determined from satellite surface reflectance products; next, an ANN for determining fractions of each surface type from satellite-derived surface reflectance is trained using a training and test dataset; then, the resulting maps of sediment-laden ice fraction are compared with satellite true-color images; finally, we present a first large-scale, pan-Arctic assessment of sediment-laden ice based on satellite data.

2. Data and methods

2.1. Modeled spectral albedo

A structural-optical model (Light et al., 1998) coupled with a four-stream multilayer discrete ordinates method radiative transfer model (Grenfell, 1991) was used to calculate surface spectral albedo for clean bare ice (clean ice), sediment-laden bare ice (sediment-laden ice), ponded ice, and ice-free open water. In this study, we consider a series of sediment-laden ice cases with sediment loads of 25, 50, 75, 100, 125, 150, 200, 300, 400, 500, 600, 700, 800, 900, and 1000 g m^{-3}. The structural-optical model incorporates information about the physical properties of the ice (specifically, brine and gas inclusion size and number densities typical of sea ice) and predicts inherent optical properties, whereas the radiative transfer model utilizes inherent optical properties, together with additional information about the boundary conditions, layer structure, and incident light field to solve the radiative-transfer equation and predict apparent optical properties.

Spectral albedos were computed based on the following experimental setups (Huck et al., 2007; Light et al., 1998). For each bare ice case, a three-layer model was used with a 0.05 m thick uppermost highly scattering layer. The particulates were assumed to be distributed evenly in the uppermost 0.25 m of the sediment-laden bare ice. Specific physical and optical properties of the three layers are given in Table 1 of Light et al. (1998). In addition, melt ponds on ice were specified to be 0.25 m deep (see Fig. 11 Perovich et al., 2003) with vertically uniform optical properties. The open water albedo was computed with the radiative transfer model assuming Fresnel reflection and refraction at the air-ocean interface and negligible (but non-zero) multiple scattering within the water column. The computed albedo is commensurate with albedos reported by Pegau and Paulson (2001). Further details are described in Huck et al. (2007) and Light et al. (1998).

2.2. MODIS surface reflectance

The latest collection (C61) of Terra/MODIS surface reflectance (MOD09GA) product at 500 m spatial resolution at seven narrow spectral bands 1–7 was downloaded from the NASA Level-1 and Atmosphere Archive and Distribution System (LAADS) Distributed Active Archive Center (DAAC) over the Arctic sea-ice region, defined here as the area northward of 60°N. For comparison with the fraction maps of sediment-laden ice, level 1A Terra/MODIS images were downloaded from the NASA Ocean Color website (https://oceancolor.gsfc.nasa.gov/). Processing from level 1A to level 2 of the MODIS images was conducted using the latest version of NASA's SeaWiFS Data Analysis System (SeaDAS 7.5.3). True-color images at 250 m spatial resolution with the spectral band combination 1–4-3 were created using the SeaDAS. Prior to analysis, the MOD09 product MODIS tiles were reprojected into a polar stereographic projection (EPSG 3413), mosaicked into daily images, and a cloud and land mask incorporated in the MOD09GA product was applied (Rösel et al., 2012).

2.3. MISR surface reflectance

In addition to MODIS surface reflectance, this study used a surface reflectance dataset derived from the Multi-angle Imaging Spectroradiometer (MISR) sensor onboard the Terra satellite. The MISR deploys nine cameras with different view angles, which provide for a near-instantaneous and high-quality sea-ice albedo data product at four narrow spectral bands (blue, green, red, and near-infrared). Daily images of bi-hemispherical reflectance (BHR) at 1 km spatial resolution at four narrow spectral bands (446, 558, 672, and 866 nm), observed by the MISR sensor, were downloaded from the Quality Assurance for Essential Climate Variables (QA4ECV) website (http://www.qa4ecv.eu/). As MISR's cloud mask over snow or sea ice is not yet sufficiently robust since MISR's spectral bands are confined to the visible and the near-infrared, this MISR BHR product employs the simultaneously acquired MODIS cloud mask (Kharbouche and Muller, 2019). In general, the measured albedo of the surface, called blue-sky albedo, is a combination of BHR and directional hemispherical reflectance (DHR). In the case of MISR, the BHR product is very close to the blue-sky albedo because of the simultaneous retrieval of a surface bi-directional reflectance factor and aerosol optical depth, and therefore the MISR BHR has been utilized as a proxy for large-scale sea-ice albedo (Kharbouche and Muller, 2019).

2.4. Surface type distinction

A spectral unmixing algorithm (Rösel et al., 2012; Tschudi et al., 2008) was used to compute fractions of each surface type. The spectral unmixing algorithm is defined by the following set of linear equations:

Table 1
Summary statistics for the best five combinations of two sediment loads for MODIS relative to hypothetical sediment-laden ice surface covering the entire area of a pixel. Rt, MPD, RMSE, and *N* represent median ratio, median absolute percent difference, root mean square error, and number of selected sediment loads, respectively.

	Sediment loads (g m^{-3})		*N*														Mean	Median
			1	2	3	4	5	6	7	8	9	10	11	12	13	14	15		
Rt	50	500	0.98	0.98	0.99	0.99	0.99	0.99	0.99	0.99	0.99	0.99	0.99	1.00	1.00	1.00	1.00	0.99	0.99
	50	600	0.98	0.98	0.99	0.99	0.99	0.99	0.99	0.99	0.99	0.99	0.99	0.99	0.99	0.99	0.99	0.99	0.99
	75	700	0.98	0.99	0.99	0.99	0.99	0.99	0.99	0.99	0.99	0.99	0.99	0.99	0.99	0.99	0.99	0.99	0.99
	25	400	0.97	0.98	0.98	0.99	0.99	0.99	0.99	0.99	0.99	0.99	0.99	0.99	1.00	1.00	1.00	0.99	0.99
	25	500	0.97	0.98	0.98	0.99	0.99	0.99	0.99	0.99	0.99	0.99	0.99	0.99	0.99	0.99	0.99	0.99	0.99
MPD (%)	50	500	2.19	1.72	1.29	1.12	1.00	0.94	0.75	0.66	0.57	0.57	0.51	0.44	0.35	0.32	0.28	0.85	0.66
	50	600	2.42	1.67	1.34	1.14	0.99	0.91	0.80	0.72	0.67	0.61	0.61	0.57	0.53	0.50	0.51	0.93	0.72
	75	700	1.82	1.30	1.06	0.97	0.93	0.86	0.85	0.80	0.77	0.77	0.78	0.72	0.75	0.69	0.66	0.91	0.80
	25	400	2.94	2.40	1.78	1.34	1.39	1.00	0.96	0.84	0.71	0.68	0.62	0.54	0.47	0.44	0.33	1.10	0.84
	25	500	3.40	2.17	1.65	1.37	1.27	1.06	0.97	0.91	0.82	0.80	0.80	0.79	0.76	0.75	0.75	1.22	0.91
RMSE ($\times 10^{-2}$)	50	500	5.72	4.04	2.87	2.09	1.75	1.49	1.30	1.20	1.09	1.01	0.94	0.93	0.88	0.86	0.83	1.80	1.20
	50	600	4.39	2.84	2.25	1.77	1.73	1.59	1.55	1.52	1.46	1.45	1.40	1.39	1.39	1.38	1.34	1.83	1.52
	75	700	3.52	2.59	2.20	2.09	2.03	2.00	1.91	1.91	1.89	1.89	1.86	1.83	1.86	1.84	1.82	2.08	1.91
	25	400	3.14	2.69	2.52	2.47	2.37	2.36	2.24	2.30	2.26	2.26	2.22	2.24	2.22	2.19	2.20	2.38	2.27
	25	500	8.22	5.73	4.20	3.52	3.01	2.18	1.95	1.68	1.36	1.29	1.18	1.05	0.94	0.85	0.75	2.53	1.68

$$\begin{bmatrix} r_{i=1,j=1} & \cdots & r_{i=5,j=1} \\ \vdots & \ddots & \vdots \\ r_{i=1,j=k} & \cdots & r_{i=5,j=k} \end{bmatrix} \begin{bmatrix} F_{i=1} \\ \vdots \\ F_{i=5} \end{bmatrix} = \begin{bmatrix} R_{j=1} \\ \vdots \\ R_{j=k} \end{bmatrix}, \quad (1)$$

$$\sum_i^5 F_i = 1, \quad (2)$$

where F_i represents the fractional area coverage of ith surface type per grid cell and R_j represents the satellite-derived surface reflectance of jth spectral band, with $r_{i,j}$ representing the model-simulated albedo of ith surface type at jth spectral band. Here, we assumed that the albedo is consistent with the surface reflectance at a single angular position. As MODIS and MISR provide surface reflectance at seven and four spectral bands, the number of spectral bands, k, corresponds to seven and four for MODIS and MISR, respectively. In this study, we estimated F_i for four major surface types: clean ice (F_C), sediment-laden ice (F_D), ponded ice (F_M), and open water (F_W). For sediment-laden ice, a greater number of sediment load categories would provide more accurate estimates for fractions of sediment-laden ice based on the spectral unmixing algorithm. In general, underdetermined systems, where the number of equations is less than the number of unknowns, have an infinite number of solutions. For this reason, we set two different sediment load categories for both MODIS and MISR so that the number of equations is the same or smaller than the number of unknowns. Although snow is also one of the major surface types in the Arctic, we did not incorporate snow into the spectral unmixing algorithms because sediment-laden ice is a typical summer-specific feature observed after snow removal through melt. Furthermore, the thin residual snow cover is mostly metamorphic coarse-grained snow exhibiting spectral albedos similar to the bare ice (Lei et al., 2012), suggesting that eliminating snow from our satellite-based approaches would have a negligible impact on their performance in estimating sediment-laden ice fractions. This set of equations was solved by a least square method using the MATLAB *lsqlin* function (R2020b, Optimization Toolbox), with lower and upper bounds of zero and one on F_i (initialized at 0.20 for each F_i) and Eq. (2) as a further constraint. Note that we confirmed that the selection of the initial value for each F_i makes no difference in the resulting fractions.

2.5. Sensitivity analyses

To evaluate the performance of our approach with two specific sediment loads for sediment-laden ice representing a wide range of sea-ice sediment loads, we conducted a sensitivity analysis using modeled spectral albedo. For the sensitivity analysis, variable combinations of sediment loads (25, 50, 75, 100, 125, 150, 200, 300, 400, 500, 600, 700, 800, 900, and 1000 g m^{-3}) and their fractions were randomly assigned to produce hypothetical surface reflectance. Underlying this analysis is the assumption that sediment-laden ice with a range of sediment loads covers the entire area, such that the areal fraction of sediment-laden ice is equal to one. The hypothetical surface reflectance was produced by the following equations:

$$\begin{bmatrix} r_{i=1,j=1} & \cdots & r_{i=N,j=1} \\ \vdots & \ddots & \vdots \\ r_{i=1,j=k} & \cdots & r_{i=N,j=k} \end{bmatrix} \begin{bmatrix} F_{i=1} \\ \vdots \\ F_{i=N} \end{bmatrix} = \begin{bmatrix} R_{j=1} \\ \vdots \\ R_{j=k} \end{bmatrix}, \quad (3)$$

$$\sum_i^N F_i = 1, \quad (4)$$

where N represents the number of randomly selected surface reflectance for sediment-laden ice with full range of sediment loads. First, $r_{i,j}$ for two different sediment loads were randomly selected out of all sediment loads (i.e., 15 sediment loads from 25 to 1000 g m^{-3}). Assuming that fractions of sediment-laden ice with the selected sediment loads satisfy Eq. (4), F_i for each sediment-laden ice category were randomly determined by the MATLAB *rand* function (R2020b). Note that the sum of F_i was enforced to be one afterward, with lower and upper bounds of zero and one, respectively. Next, the hypothetical areal surface reflectances were computed from $r_{i,j}$ and F_i using Eq. (3). These procedures were repeated 1000 times, and then F_i were estimated by spectral unmixing algorithms for MODIS and MISR bands. After 1000 iterations, the performance of the spectral unmixing algorithms for estimating fractions of sediment-laden ice was evaluated by statistical metrics described in section 2.7. We repeated the entire procedure for variable numbers of the randomly selected surface type (N) from two to 15 with random fractions to ensure the stable performance of our approach for a complex mosaic of a broader range of sediment-laden ice. Finally, the optimum combinations of two sediment loads for MODIS and MISR were determined based on the statistical metrics. The surface types used here were selected randomly for each repeat by the MATLAB *randperm* function (R2020b).

Once we determined the best combinations of two sediment loads for MODIS and MISR, this study further examined sensitivity of the MODIS- and MISR-based spectral unmixing algorithms for mosaic of ice surface types. For this sensitivity analysis, hypothetical areal surface reflectance was generated using a variety of ice surface types, i.e., not only sediment-laden ice but also other surface types, including clean ice, ponded ice, and open water (i.e., 18 surface types in total). The procedure for this sensitivity analysis was the exact same as the aforementioned approach for determining the best combination of sediment loads, except the total number of ice surface types increased from 15 to 18.

2.6. Artificial neural network

As this study examined satellite images with high spatial resolution, extracting surface types with the spectral unmixing algorithm based on a least square method was a time-consuming process. To overcome this obstacle, we developed an ANN for mapping sediment-laden ice using satellite-derived surface reflectance. Among the different types of ANNs, a multi-layered perceptron (MLP) has been chosen for its properties as universal approximator of any continuous and derivable function (Rumelhart et al., 1986). MLPs are a class of feed-forward ANNs that consist of an input layer, one or more hidden layers, and an output layer (Fig. 3). These layers contain neurons that are connected to the adjacent layers and able to exchange information through weighted connections (Atkinson and Tatnall, 1997). The development of MLPs establishes these weights by a supervised learning process using predefined outputs corresponding to the input data. In this study, we constructed MLPs with two hidden layers using the MATLAB *train* function (R2020b, Deep Learning Toolbox). A set of the optimal numbers of neurons in these two hidden layers was determined by trial-and-error, i.e., the number of neurons in each hidden layer were varied between five and 50 with five-increment steps. Then, the optimal number of neurons for each layer was determined based on the performance of the trained ANNs (see section 2.7). The sigmoid transfer function was used by the neurons in the two hidden layers, whereas the softmax transfer function was used for the output layer to constrain the sum of the output values to be exactly equal to one with a set of lower and upper bounds of zero and one, respectively.

To maximize the geographic and seasonal coverages of datasets for the ANN development, we prepared a manageable dataset as a subset of the overall MOD09GA data archive for 2020 during the six months of north polar daylight (from April to September). First, a list of days with cloud-free surface reflectances out of the overall MOD09GA data archive for 2020 was compiled for each pixel. Out of the list, cloud-free surface reflectances per pixel of ten randomly selected days were assigned to a dataset used for training, validating, and testing ANNs. If a pixel had less than ten days with cloud-free surface reflectances, all cloud-free spectra were included in the dataset. This approach ensured that a location or a season with very few data points was still represented in the dataset, or conversely prevented regions with many valid data or seasons with the most favorable atmospheric conditions from dominating the training process (Mélin and Vantrepotte, 2015). The resulting dataset for the

ANN development amounted to over 16 million spectra, and the fractional coverages of each surface type for each spectrum were computed by applying the spectral unmixing algorithms to the dataset. Subsequently, based on the procedure proposed in Kulp and Strauss (2018), the dataset was split into three subsets: a training subset (70%), a validation subset (15%), and a test subset (15%). In this study, ANNs were trained using the MATLAB *train* function. A common problem encountered in machine learning is that the ANN model does not generalize well from training data to unseen data because of overfitting of the training data (Robilliard and Fonlupt, 2002). When an ANN begins to overfit the data, the error on the validation subset typically begins to rise. To avoid overfitting, the errors on the validation subset were monitored during the training process. The training was stopped after six consecutive increases in validation error, and the weights corresponding to the minimum of the error on the validation subset were returned as the resulting ANNs. Finally, the performance of the best ANN was validated using the test subset.

2.7. Performance validation

The performance of the spectral unmixing algorithm and ANNs were evaluated based on three statistical metrics: the median ratio (Rt), median absolute percent difference (MPD), and root mean square error (RMSE) between the least-square-based and the ANN-based values. Particularly, Rt, MPD, and RMSE were calculated as follows:

$$\mathrm{Rt} = \mathrm{median}\left(\frac{Y_n}{X_n}\right), \tag{5}$$

$$\mathrm{MPD} = \mathrm{median}\left(\left|\frac{X_n - Y_n}{X_n}\right| \times 100\right), \tag{6}$$

$$\mathrm{RMSE} = \sqrt{\frac{1}{N}\sum_{n=1}^{N}(\mathrm{X}_n - Y_n)^2}, \tag{7}$$

where X_n and Y_n represent the nth input and output values, respectively.

3. Results

3.1. Spectral albedos for different surface types

The model-simulated spectral albedos for four surface types for wavelengths 400–2400 nm are shown in Fig. 4. Each surface type has a unique spectral shape and magnitude of the albedo. For example, the spectral albedo of clean ice exhibited a more pronounced peak at shorter wavelengths (~470 nm) compared to the flatter maximum at longer wavelength (~850 nm) for sediment-laden ice. As sediments are the dominant absorber in the visible range, the difference in albedos between clean and sediment-laden ice was most distinct at shorter wavelengths. Towards longer wavelengths (>1000 nm) these differences diminish because absorption by the ice becomes increasingly dominant with greater wavelengths, reducing the relative importance of absorption by sediments. The lowest albedo was found for open water, which exhibited a negligible spectral variation with albedo values of ~0.1 throughout the wavelength 400–2400 nm.

3.2. Performance of spectral unmixing algorithms

Using the modeled spectral albedo of sediment-laden ice for 15 different sediment loads, we generated hypothetical ice surfaces consisting entirely of sediment-laden ice with a wide variety of sediment loads. The predicted surface reflectance spectra accompanying the resulting mosaics of sediment-laden ice were then used to compute areal fractions of sediment-laden ice based on the spectral unmixing algorithms with variable combinations of two categories for sediment-laden ice. Table 1 shows a comparison of the estimated and hypothetical areal fractions for MODIS surface reflectance, suggesting that the combination of sediment-laden ice with sediment loads of 50 and 500 g m^{-3} exhibited the best performance for estimating areal fractions of sediment-laden ice. Indeed, the spectral unmixing algorithm for MODIS with two sediment-laden ice categories of 50 and 500 g m^{-3} estimates areal fractions of hypothetical sediment-laden ice surfaces correctly with average Rt, MPD, and RMSE of 0.99, 0.85%, and 1.80 × 10^{-2}, respectively (Table 1).

Given the promising performance of the spectral unmixing algorithm, we examined the sensitivity of this approach to identify the optimal combination of two different sediment loads in capturing variable mosaics of different surface types based on MODIS surface reflectances. The performances of the spectral unmixing algorithm for a wide range of hypothetical complex mosaics of surface types are shown in Table 2. The areal fraction of sediment-laden ice yielded an MPD and RMSE of 1.90% and 8.11 × 10^{-2} for the simplest hypothetical surface pattern ($N = 2$), whereas those for the most complex pattern ($N = 18$) were 0.57% and 0.76 × 10^{-2}. Across all four surface types, the maximum MPD and RMSE were 6.80% and 8.11 × 10^{-2}, respectively. In addition, Rt for each surface type was close to 1.00 across the varying complexity in surface. Moreover, the mean ratios and mean percent differences also showed consistent results with Rt and MPD (e.g., sediment-laden ice yielded the mean ratio and mean percent difference of 1.00 and 0.61% for the most complex pattern), suggesting these statistics can be seen as representative values. These statistics indicate that the spectral unmixing algorithm for MODIS successfully retrieved areal fractions of each surface type and sediment loads even for a complex mosaic of the ice surface. Note that the spectral unmixing algorithm yielded negligible areal fraction of sediment-laden ice (<0.01) for the sediment-free hypothetical ice surface and marginal ice zone (i.e., mosaic of clean ice, ponded ice, and open water, except sediment-laden ice).

The same procedures were applied to the spectral unmixing algorithm for MISR. In accordance with MODIS data analysis, the combination of two sediment loads of 50 and 500 g m^{-3} performed the best to estimate areal fractions of sediment-laden ice using the spectral unmixing algorithm for MISR surface reflectance (Table 3). However, the resulting areal fraction of sediment-laden ice contained substantial errors compared with those of the MODIS-based approach. As the sum of each areal fraction was constrained to equal 1, such estimation errors in the areal fraction of sediment-laden ice result in under- or overestimating of other surface types. In fact, the MISR-based approach in the mosaic experiment demonstrated poorer estimation accuracy than the MODIS-based approach across all of the surface types (Table 4). Overall, MPD and RMSE for the areal fraction of sediment-laden ice in the most complex mosaic ice surface ($N = 18$) were 2.86% and 3.36 × 10^{-2}, which are more than three times as large as those for the MODIS-based approach. Overall, the three statistics for the MISR-based approach yielded relatively poor results across all the four surface types (Table 4). These results clearly indicate that MODIS data are more suited for the spectral unmixing approach because more spectral bands for capturing spectral variations are available when comparing with MISR data.

3.3. Remote estimation of surface types

To further verify the performance our approach, we compared maps of areal fractions of each surface type derived from the spectral unmixing algorithm for MODIS surface reflectance with Terra/MODIS true-color images for a region of near Point Barrow shown in Fig. 2. On April 19 (Fig. 5), the fraction maps show that clean ice was the dominant surface type (>0.8) over the area. It is important to recall that snow-covered areas were classified as clean ice because snow was not specified in the spectral unmixing algorithm in this study. Therefore, the areal fraction of clean ice was largely composed of snow coverage at this time

Table 2
Performances of the MODIS-based spectral unmixing algorithm for a wide range of hypothetical mosaics of surface types. Rt, MPD, RMSE, and *N* represent median ratio, median absolute percent difference, root mean square error, and number of selected surface types, respectively. F_C, F_D, F_P, and F_W represent areal fractions of clean ice, sediment-laden ice, ponded ice, and open water.

N	Rt				MPD (%)				RMSE ($\times 10^{-2}$)			
	F_C	F_D	F_P	F_W	F_C	F_D	F_P	F_W	F_C	F_D	F_P	F_W
2	0.99	0.98	0.93	1.00	1.41	1.90	1.47	0.70	6.48	8.11	6.06	3.94
3	0.96	0.99	0.90	0.98	5.51	2.06	2.23	1.27	4.46	4.83	6.55	3.76
4	0.97	0.99	0.92	0.98	5.24	1.70	2.07	1.62	2.98	3.73	5.22	3.69
5	0.97	0.99	0.95	0.96	6.80	1.65	1.95	1.60	2.64	3.01	4.60	3.73
6	0.98	0.99	0.95	0.98	6.41	1.41	2.28	1.46	2.16	2.53	4.31	3.14
7	0.97	0.99	0.94	0.97	6.05	1.39	2.37	1.91	1.88	2.22	4.15	3.63
8	0.97	0.99	0.98	0.98	6.42	1.39	1.79	1.85	1.63	2.01	3.22	2.96
9	0.96	1.00	0.99	0.98	5.99	1.24	2.08	2.19	1.36	1.89	2.96	3.01
10	0.96	1.00	1.01	0.99	6.48	1.22	2.11	1.93	1.33	1.71	2.88	2.88
11	0.96	1.00	1.01	0.99	6.21	1.11	1.87	2.01	1.24	1.59	2.28	2.87
12	0.97	1.00	1.01	0.99	5.47	1.03	1.95	1.80	1.00	1.44	2.45	2.58
13	0.99	1.00	1.04	1.02	4.47	0.92	2.00	1.96	0.83	1.34	2.09	2.41
14	0.96	1.00	1.05	1.05	5.50	0.84	1.81	1.80	0.95	1.24	1.84	2.36
15	0.98	1.00	1.03	1.06	3.31	0.72	1.70	1.83	0.72	1.12	1.76	2.15
16	0.98	1.00	1.04	1.07	3.84	0.66	1.96	2.14	0.69	0.94	1.70	2.22
17	0.98	1.00	1.06	1.10	3.09	0.58	1.81	2.19	0.70	0.85	1.51	2.29
18	0.97	1.00	1.05	1.08	3.31	0.57	1.49	1.91	0.60	0.76	1.39	1.62

Table 3
Summary statistics for the best five combinations of two sediment loads for MISR relative to hypothetical sediment-laden ice surface covering the entire area of a pixel. Rt, MPD, RMSE, and *N* represent median ratio, median absolute percent difference, root mean square error, and number of selected sediment loads, respectively.

	Sediment loads (g m^{-3})		*N*															Mean	Median
			1	2	3	4	5	6	7	8	9	10	11	12	13	14	15		
Rt	50	500	0.95	0.97	0.97	0.98	0.98	0.98	0.99	0.99	0.99	0.99	0.99	0.99	0.99	0.99	0.99	0.98	0.99
	50	600	0.95	0.96	0.97	0.98	0.98	0.98	0.99	0.99	0.99	0.99	0.99	0.99	0.99	0.99	0.99	0.98	0.99
	75	700	0.96	0.97	0.98	0.98	0.98	0.98	0.98	0.98	0.98	0.99	0.99	0.99	0.99	0.99	0.99	0.98	0.98
	25	400	0.96	0.97	0.97	0.98	0.98	0.98	0.98	0.98	0.98	0.98	0.98	0.98	0.98	0.98	0.99	0.98	0.98
	25	500	0.94	0.96	0.97	0.98	0.98	0.98	0.98	0.98	0.98	0.98	0.99	0.98	0.99	0.99	0.99	0.98	0.98
MPD (%)	50	500	4.62	3.38	2.62	2.18	1.85	1.80	1.38	1.23	1.20	1.00	0.92	0.79	0.67	0.58	0.51	1.65	1.23
	50	600	5.49	4.08	3.02	2.40	1.99	1.69	1.39	1.21	1.17	1.05	0.96	0.84	0.72	0.60	0.51	1.81	1.21
	75	700	4.44	3.43	2.40	2.33	2.17	1.84	1.68	1.59	1.51	1.37	1.33	1.26	1.14	1.10	1.09	1.91	1.59
	25	400	3.54	3.05	2.58	2.44	2.12	2.18	1.97	2.02	1.89	1.87	1.76	1.69	1.57	1.58	1.40	2.11	1.97
	25	500	6.04	4.06	2.85	2.35	2.16	1.97	1.74	1.67	1.62	1.55	1.47	1.53	1.45	1.47	1.48	2.23	1.67
RMSE ($\times 10^{-2}$)	50	500	6.85	5.25	4.26	3.62	3.24	2.83	2.51	2.13	2.12	2.02	1.82	1.82	1.71	1.66	1.64	2.90	2.13
	50	600	5.96	4.90	4.11	3.73	3.37	3.24	3.14	3.00	2.97	2.88	2.78	2.80	2.75	2.77	2.74	3.41	3.00
	75	700	8.92	7.09	6.64	5.39	4.68	4.07	3.55	2.97	2.75	2.64	2.00	1.85	1.33	1.26	0.95	3.74	2.97
	25	400	10.27	7.88	6.49	5.87	4.82	4.17	3.61	3.02	2.72	2.34	2.03	1.88	1.51	1.38	1.34	3.96	3.02
	25	500	10.54	7.52	6.24	5.52	4.62	3.77	3.43	2.90	2.47	2.28	2.16	2.06	2.01	1.98	1.95	3.96	2.90

Table 4
Performances of the MISR-based spectral unmixing algorithm for a wide range of hypothetical mosaics of surface types. Rt, MPD, RMSE, and *N* represent median ratio, median absolute percent difference, root mean square error, and number of selected surface types, respectively. F_C, F_D, F_P, and F_W represent areal fractions of clean ice, sediment-laden ice, ponded ice, and open water.

N	Rt				MPD (%)				RMSE ($\times 10^{-2}$)			
	F_C	F_D	F_P	F_W	F_C	F_D	F_P	F_W	F_C	F_D	F_P	F_W
2	1.00	0.97	0.94	1.00	4.34	3.83	4.39	3.89	8.13	9.76	6.07	4.53
3	0.97	0.98	0.92	0.99	6.69	3.26	5.82	4.16	5.45	8.15	5.40	3.92
4	0.96	0.98	0.91	1.00	8.75	2.87	8.62	4.26	3.33	7.53	5.15	4.46
5	0.95	0.98	0.91	1.04	9.33	2.91	8.34	4.96	3.19	6.93	4.97	4.79
6	0.91	0.98	0.92	1.05	9.28	2.93	8.48	5.32	2.91	6.20	4.65	4.50
7	0.91	0.98	0.91	1.11	9.16	3.13	9.37	5.48	2.74	6.22	4.10	4.00
8	0.92	0.98	0.92	1.12	9.69	2.92	9.56	5.98	2.65	5.92	3.95	3.93
9	0.92	0.98	0.94	1.11	9.31	3.51	9.71	6.18	2.38	5.78	3.73	3.60
10	0.90	0.98	0.98	1.13	9.18	3.05	9.42	6.28	2.19	5.14	3.11	3.55
11	0.92	0.98	1.03	1.16	9.67	3.11	9.87	6.76	2.07	4.95	3.20	3.30
12	0.92	0.98	1.07	1.19	9.81	3.12	9.36	8.08	1.85	4.60	3.03	3.35
13	0.92	0.97	1.11	1.20	8.70	3.17	9.88	8.43	1.74	4.43	2.71	3.25
14	0.94	0.98	1.09	1.16	7.91	2.90	9.54	6.91	1.62	4.10	2.69	2.76
15	0.92	0.98	1.13	1.17	9.32	2.95	9.39	6.90	1.54	3.95	2.53	2.74
16	0.94	0.97	1.10	1.17	7.31	2.86	8.42	6.93	1.35	3.62	2.14	2.58
17	0.97	0.97	1.11	1.20	5.73	2.86	8.18	8.24	1.14	3.58	2.15	2.77
18	0.94	0.97	1.06	1.18	6.92	2.86	7.05	7.71	1.17	3.36	1.78	2.54

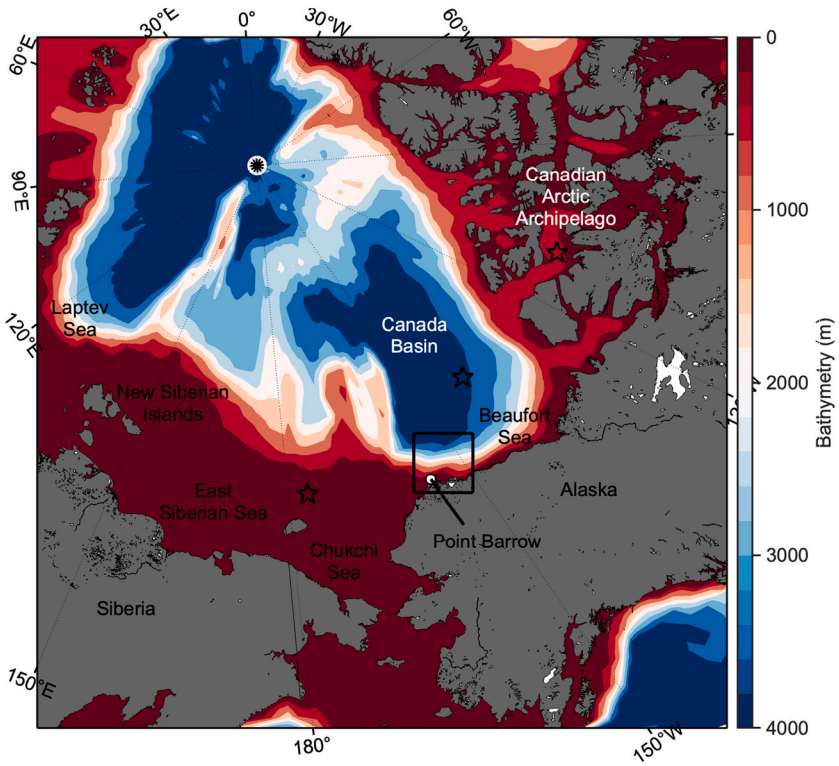

Fig. 2. Bathymetric map with place names. The black box delineates the region of interest for a comparison between the satellite-derived fraction maps with the corresponding Terra/MODIS true-color images (see Figs. 6–10). Yellow stars represent the centers of 25 × 25 pixel (12.5 × 12.5 km) data subsets used to analyze seasonal variations of the different surface types (see Fig. 12). (For interpretation of the references to color in this figure legend, the reader is referred to the web version of this article.)

of year, resulting in consistently white color in the Terra/MODIS true-color image (Fig. 5a). These facts resulted in relatively small (~0.8) R^2 (Fig. 5f), as a measure of goodness of fit of the spectral unmixing algorithm. In addition, the true-color image shows a thin gray line in the top left part of the image around 72–73°N and 156–152°W, presumably because of the presence of a narrow lead. We detected a relatively high fraction (>0.3) of open water in the area (Fig. 5e), suggesting our approach would detect the lead in the ice region even at sub-pixel width (i.e., less than 500 m width). Similarly, a quite small but non-zero fraction (<0.1) of open water distributed widely in the area at some distance to the coast, presumably representing the presence of narrow sea-ice leads.

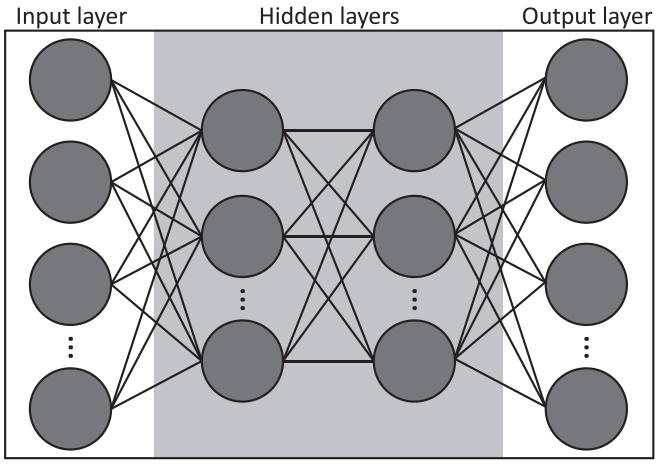

Fig. 3. Structure of the ANN with two hidden layers. Gray circles represent neurons, and solid lines are connections with weights from one neuron to another neuron in the adjacent layer. Four neurons in the input and output layers represent the surface reflectance and the fractions of surface types, respectively. The ANN developed in this study contains two hidden layers with 45 neurons for the first hidden layer and 35 neurons for the second hidden layer; for illustration purposes the figure only shows an excerpt for each layer.

With removal of snow cover as a result of surface melt, clean ice coverages increased substantially by June 13 (Fig. 6). Indeed, R^2 yielded almost 1.00 across the area (Fig. 6f), suggesting our spectral unmixing algorithm successfully captured spectral variations in ice surface reflectance with the four major surface types (i.e., clean ice, sediment-laden ice, ponded ice, and open water). Clean ice (Fig. 6b) was the dominant surface type over a wide area (>0.8), whereas particularly high areal fractions (>0.6) of sediment-laden ice were found in greater vicinity of the coast (Fig. 6c). These spatial patterns were consistent with the distributions of white and brownish ice shown in the true-color image (Fig. 6a). Additionally, we observed patchy areas with high fractions of ponded ice (Fig. 6d) along the cloud shadow (Fig. 6a) surrounded by high fractions of clean ice (Fig. 6b). Moreover, the true-color image indicates that sea-ice leads were likely distributed widely around 71–72°N and 152–155°W, while most of these areas were masked out by the MODIS cloud mask. It is noteworthy that the remnants of those sea-ice lead areas were successfully distinguished as open water areas (Fig. 6e).

The true-color image from July 24, 2006 (Fig. 7a), shows extensive areas of brownish ice in the west, suggesting a more wide-spread distribution of sediment-laden ice. Indeed, the spatial distribution of brownish ice in the true-color image and the high fraction of sediment-laden ice in the corresponding areal fraction map agree well (Fig. 7c). Furthermore, aerial photographs taken of sediment-laden ice near Point Barrow on June 30, 2006 (Fig. 1) serve as ground-truth observations that provide further confirmation for the time and region of interest. We also observed moderate areal fractions of open water over the ice-covered areas (Fig. 7e). Although ice-free areas were not distinguishable in the true-color images, open water might have existed in the ice-covered areas at finer spatial scales invisible from the true color image with 250 m spatial resolution. The spatial distribution of R^2 showed small values along the coast, where very turbid (i.e., brown colored) waters were expected. As our spectral unmixing algorithm specified only clean seawater for ice-free surface types, such turbid water associated with high concentrations of suspended materials was accompanied by poor

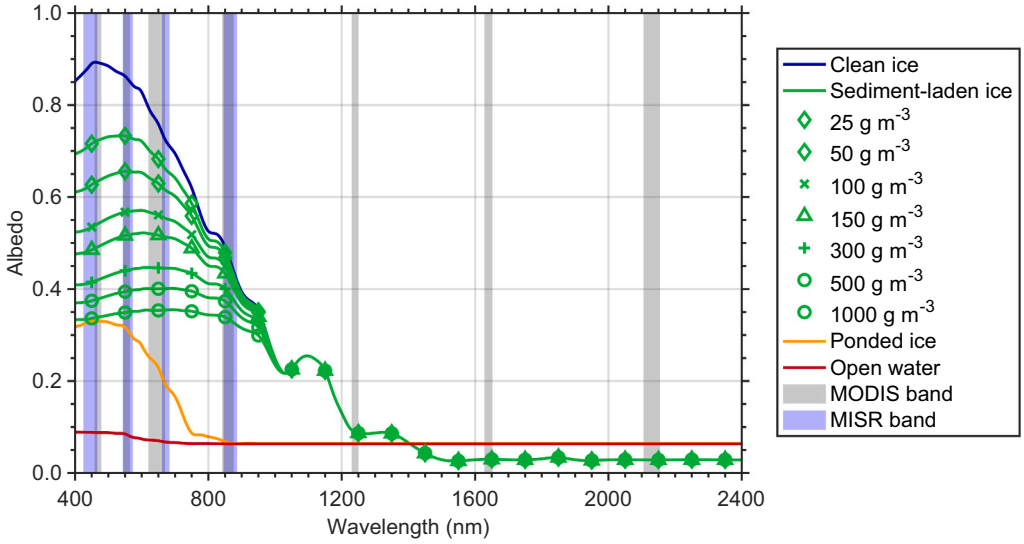

Fig. 4. Modeled spectral albedos for the four surface types (i.e., clean ice, sediment-laden ice, ponded ice, open water) for wavelengths 400–2400 nm under direct incident illumination with solar zenith angle 50°. Each green symbol represents sediment loads between 25 and 1000 g m^{-3}; for illustration purposes the figure only shows an excerpt for 7 sediment loads out of the full range of sediment loads considered in this study. The blue and gray bars represent the range of the four MISR bands and seven MODIS bands, respectively. (For interpretation of the references to color in this figure legend, the reader is referred to the web version of this article.)

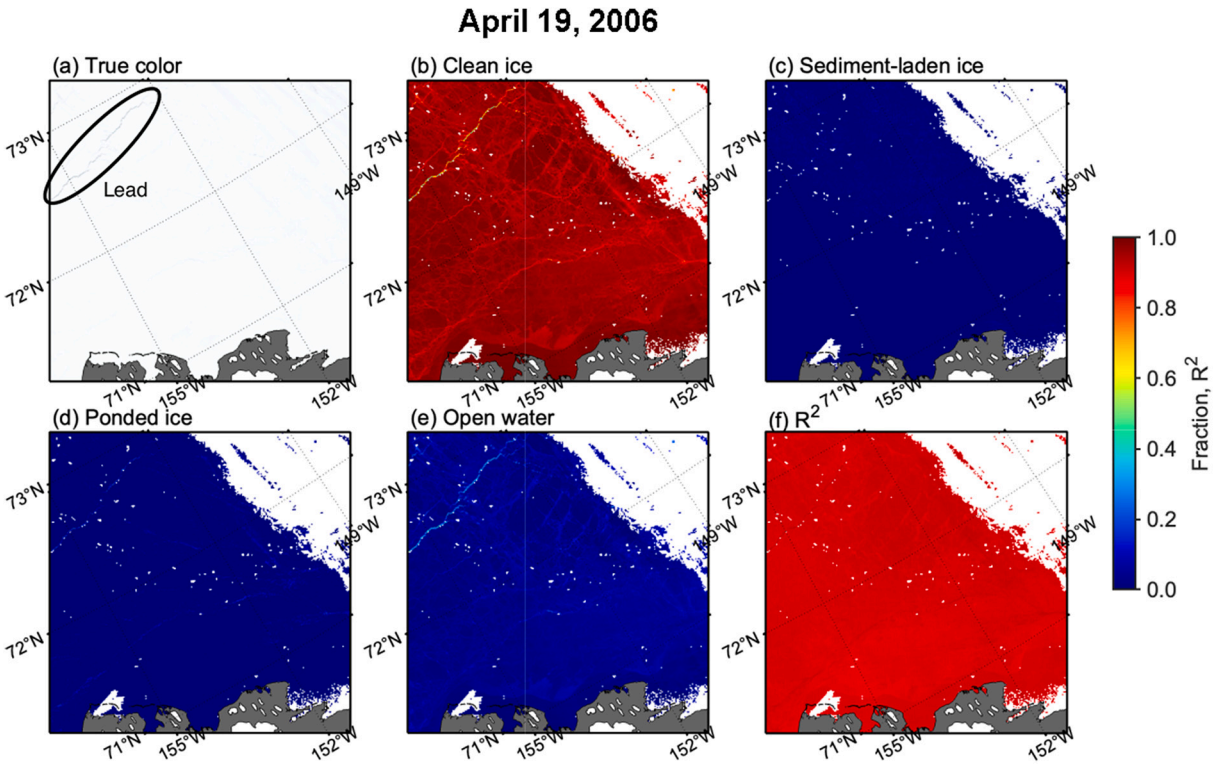

Fig. 5. (a) Terra/MODIS true-color image and maps of areal fractions of (b) clean ice, (c) sediment-laden, (d) ponded ice, (e) open water, and (f) R^2 of the spectral unmixing algorithm near Point Barrow on April 19, 2006. The areal fractions were derived by the MODIS-based spectral unmixing algorithm. White pixels in (b)–(f) were identified as cloud covered by the MODIS cloud mask.

goodness of fit by the spectral unmixing algorithm.

Spatial patterns of the dominant surface type on April 19, June 13, and July 24, 2006 are shown in Fig. 8. As melt progresses, the proportion of sediment-laden ice dominated areas increased. More specifically, the proportion of sediment-laden ice dominated areas reached 56.6% near Point Barrow on July 24, 2006, whereas those on April 19 and June 13, 2006, were 0.0% and 12.1%, respectively. Sediment-laden ice was the dominant surface type in coastal areas on June 13, primarily as part of the landfast ice. After break-up and displacement of the landfast ice, on July 24 the vicinity of Point Barrow was characterized as marginal ice zone associated with a open ice pack, with pixels dominated by sediment-laden ice widely distributed across the area. Among the extensive areas with a dominance of sediment-laden ice, we found large patches of open water-dominant pixels around 71–72°N and 154–156°W. Comparing the true-color image (Fig. 8c) and map of the dominant surface type (Fig. 8f), these patches corresponded well with the particularly dark areas in the true-color image. The pixels in the marginal ice zone would have contained both ice-covered area and open water area. As a higher proportion of open water results in darker color in the true-color image, the dark and less dark pixels in the sediment-laden ice area would have been associated with more and less open water area within the pixel, respectively. It is noteworthy that ponded

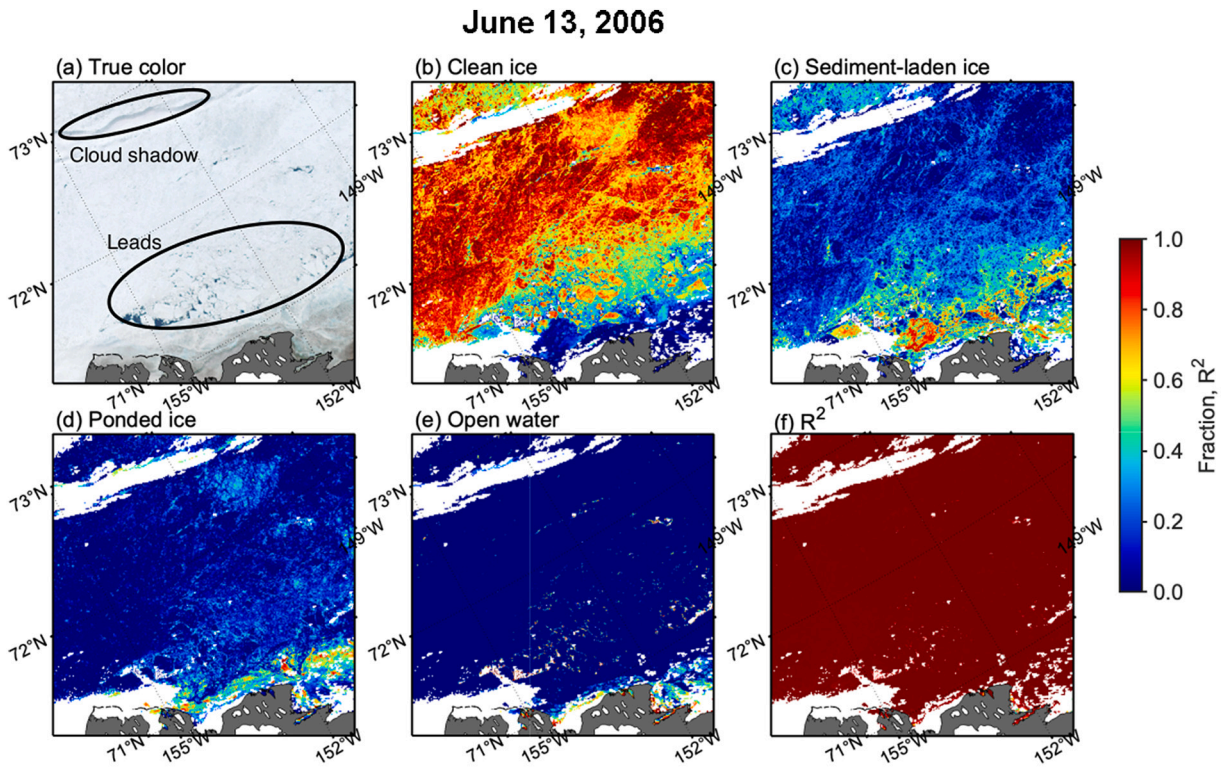

Fig. 6. (a) Terra/MODIS true-color image and maps of areal fractions of (b) clean ice, (c) sediment-laden, (d) ponded ice, (e) open water, and (f) R^2 of the spectral unmixing algorithm near Point Barrow on June 13, 2006. The areal fractions were derived by the MODIS-based spectral unmixing algorithm. White pixels in (b)–(f) were identified as cloud covered by the MODIS cloud mask.

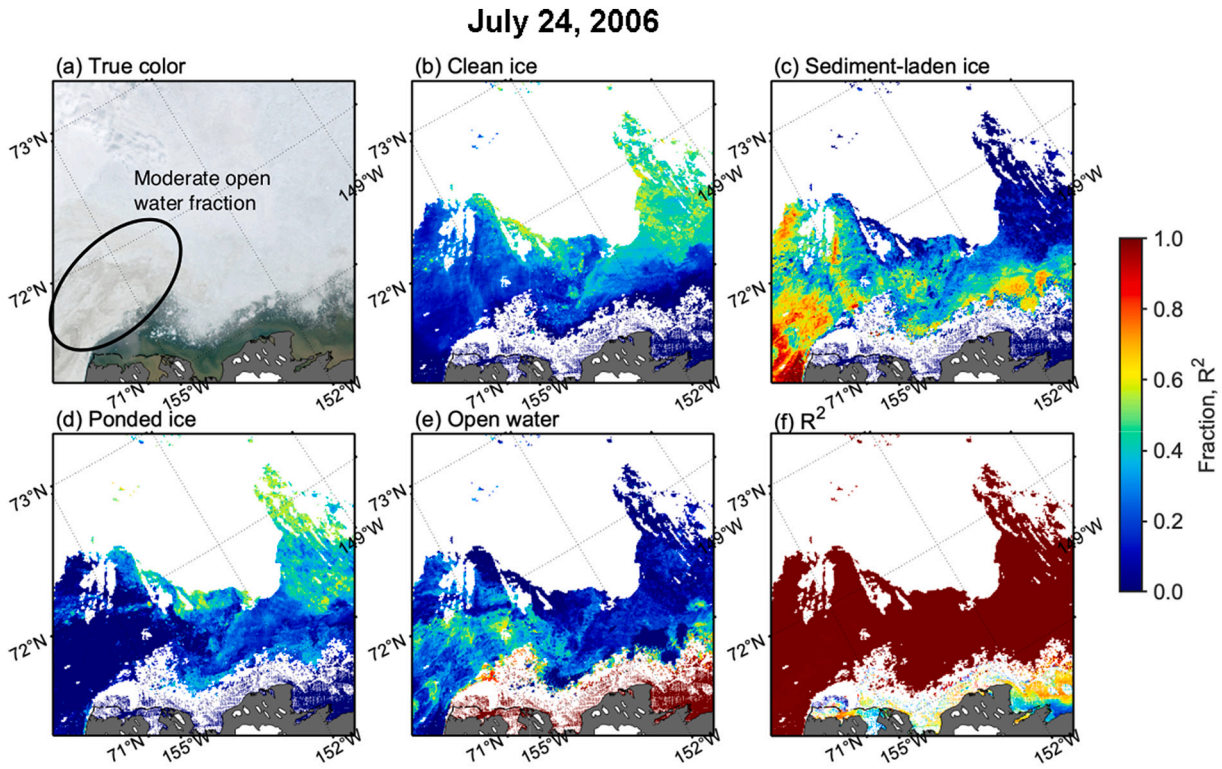

Fig. 7. (a) Terra/MODIS true-color image and maps of areal fractions of (b) clean ice, (c) sediment-laden, (d) ponded ice, (e) open water, and (f) R^2 of the spectral unmixing algorithm near Point Barrow on July 24, 2006. The areal fractions were derived by the MODIS-based spectral unmixing algorithm. White pixels in (b)–(f) were identified as cloud covered by the MODIS cloud mask.

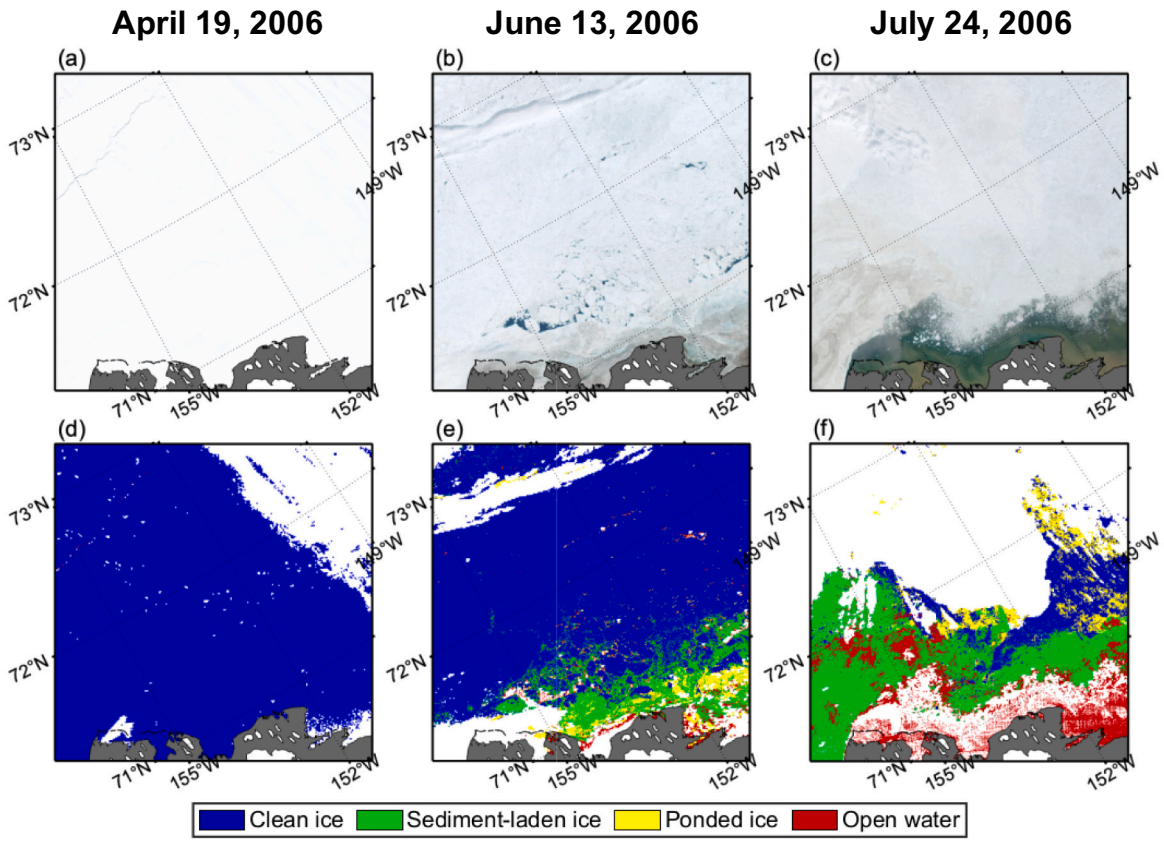

Fig. 8. (a–c) Terra/MODIS true-color images and (d–f) maps of the dominant surface type near Point Barrow on April 19, June 13, and July 24, 2006. White pixels in (d)–(f) were identified as cloud covered by the MODIS cloud mask.

ice was a less prominent surface type near Point Barrow during the time of year examined in this study (Fig. 8d–f).

3.4. Comparison between results derived from MISR and MODIS

The areal fractions of sediment-laden ice derived by the spectral unmixing algorithms for the MODIS and MISR surface reflectance and differences in areal fractions between these two sensors are shown in Fig. 9. The MODIS surface reflectance allowed for accurate derivation of areal sediment-laden ice fractions (Table 2), whereas the MISR-based approach was associated with larger errors in estimating sediment-laden ice fraction and other surface types (Table 4). On April 19, the areal fraction maps showed negligible differences for sediment-laden ice fractions (Fig. 9g), because clean ice was the dominant surface type (Fig. 8d) with sediment-laden ice of small consequence. With sediment-laden ice exposed at the ice surface as a result of surface melt, we found clear differences between the two approaches in capturing sediment-laden ice areal fractions. For example, the MODIS-based approach yielded smaller but distinct areal fractions (<0.3) in a zone at some distance to the coast on June 13 (Fig. 9b), whereas the MISR-based approach observed no or negligible fractions (<0.1) in the corresponding area (Fig. 9e). On July 24, extensive areas with larger areal fractions of sediment-laden ice were found for the MISR-derived values (>0.8) compared to those derived from MODIS (Fig. 9i). These differences in the resulting areal fraction of sediment-laden ice highlight the advantage of the larger number of available spectral bands (seven and four bands for MODIS and MISR, respectively) in capturing spectral features associated with heterogeneous ice surfaces. Note that comparisons in areal fractions derived from MODIS surface reflectance using only four spectral bands in the visible range with those derived from MISR showed smaller differences between the two (Fig. 10), suggesting the major factor producing the differences in areal fractions derived from MODIS and MISR was not related to sensor-specific features but the number of available spectral bands for these sensors.

3.5. ANN training and validation

We trained 100 ANNs to determine the optimal number of neurons in the two hidden layers. The resulting performance of the ANNs indicated that the optimal number of neurons was 45 and 35 in the first and second hidden layers, respectively. Comparisons of the values obtained from the least squares method and the ANN showed good agreements for each surface type (Fig. 11). For sediment-laden ice, the ANN retrievals were associated with an MPD and RMSE of 0.233% and 3.05×10^{-4}, respectively. In addition, Rt for sediment-laden ice was 1.00, suggesting accurate estimates of the fraction of sediment-laden ice with negligible bias. These statistics highlight the outstanding performance of the ANN (Fig. 11).

3.6. Seasonal variations in satellite-derived sediment-laden ice areal fractions

Fig. 12 shows seasonal variations in the areal fractions of each surface type for April through September 2020 for three different subregions in the East Siberian Sea, Canada Basin, and the Canadian Arctic Archipelago (see Fig. 2 for exact locations). The areal fractions of sediment-laden ice yielded maximum values of 0.58, 0.50, and 0.16 in the East Siberian Sea, Canada Basin, and Canadian Arctic Archipelago, respectively. Sediment-laden ice was often the predominant ice surface type in the East Siberian Sea and Canada Basin, particularly in the late melt stage when ice melt progressed and matured in summer. Although the areal fractions of sediment-laden ice in the East Siberian Sea and

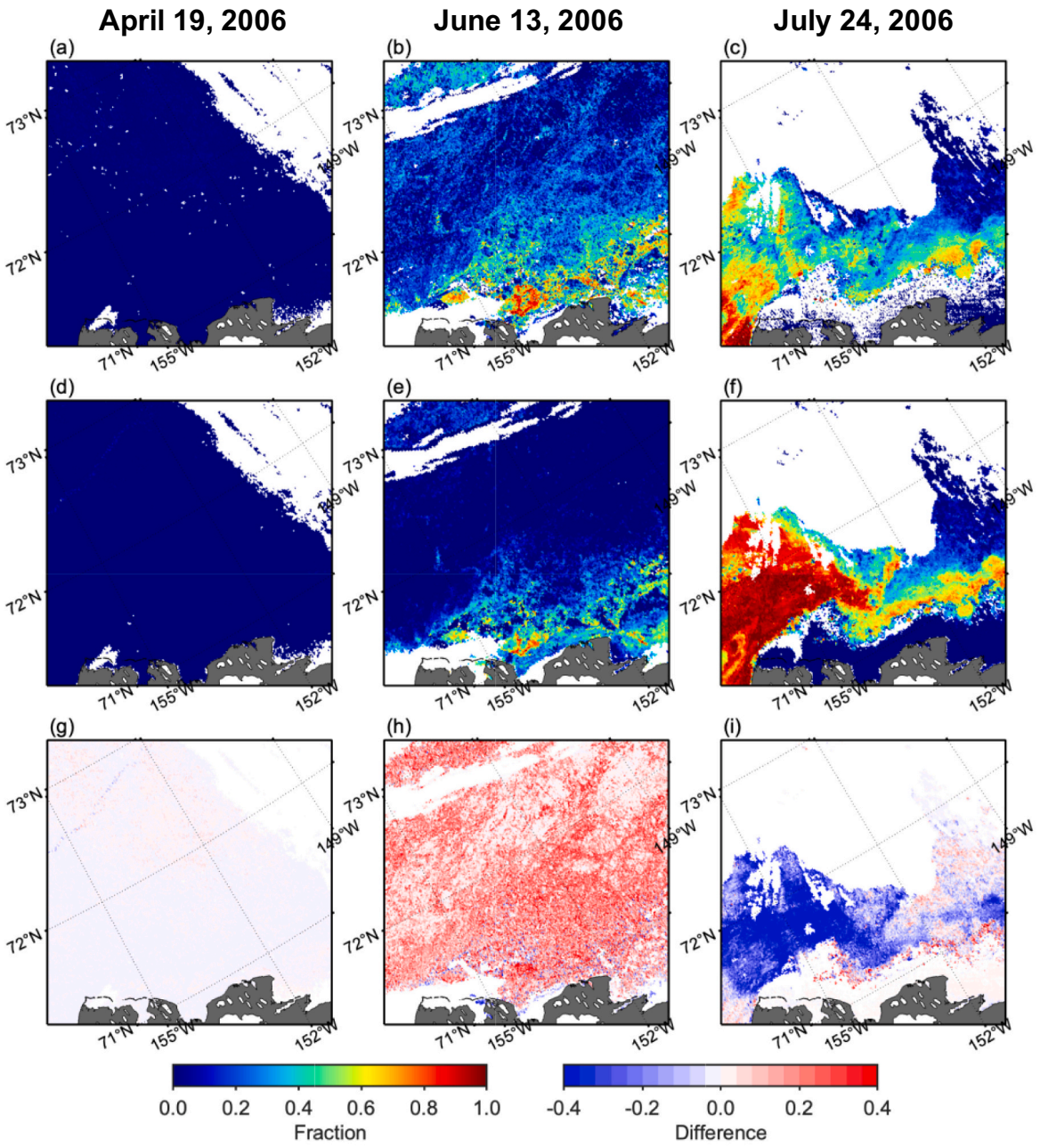

Fig. 9. Spatial patterns in areal fractions of sediment-laden ice retrieved by spectral unmixing algorithms for (a–c) MODIS surface reflectance using seven bands in the visible and near-infrared ranges, (d–f) MISR surface reflectance, and (g–i) differences in the areal fractions between the two scenes near Point Barrow on April 19, June 13, and July 24, 2006. White pixels were identified as cloud covered by the MODIS cloud mask.

Canadian Arctic Archipelago were reasonable, that of Canada Basin was likely to be too high. Indeed, the areal fraction of sediment-laden ice in the Canada Basin accounted for more than 50% of sea ice in late summer and early fall. The sources of error associated with potential misclassification are discussed in greater depth below. The ponded-ice fractions remained low (<0.2) during most of the period in the East Siberian Sea and Canada Basin, whereas a maximum value of 0.57 was observed on August 14 in the Canadian Arctic Archipelago. Larger proportions of open water were observed during late summer in all three regions. Particularly, open water accounted for close to 100% of areal fraction in the East Siberian Sea in August–September, suggesting that little or no sea ice remained in this area.

Maps for every other eight-day averaged fractions of sediment-laden ice are shown in Fig. 13. At the pan-Arctic scale, sediment-laden ice was widely distributed in coastal areas, particularly over the Siberian, Chukchi, and Beaufort shelves. Indeed, sediment-laden ice was the dominant surface type over a wide area of the coastal areas (Fig. 14). Moreover, small but non-negligible fractions (<0.2) of sediment-laden ice were found at high latitudes in later summer, where clean or ponded ice were the dominant surface types throughout the period. In contrast, clean ice was registered as the dominant surface type throughout the Arctic in spring to early summer. In the central Arctic, clean ice dominated the surface even in summer, and ponded ice was also identified as the dominant surface type in some areas.

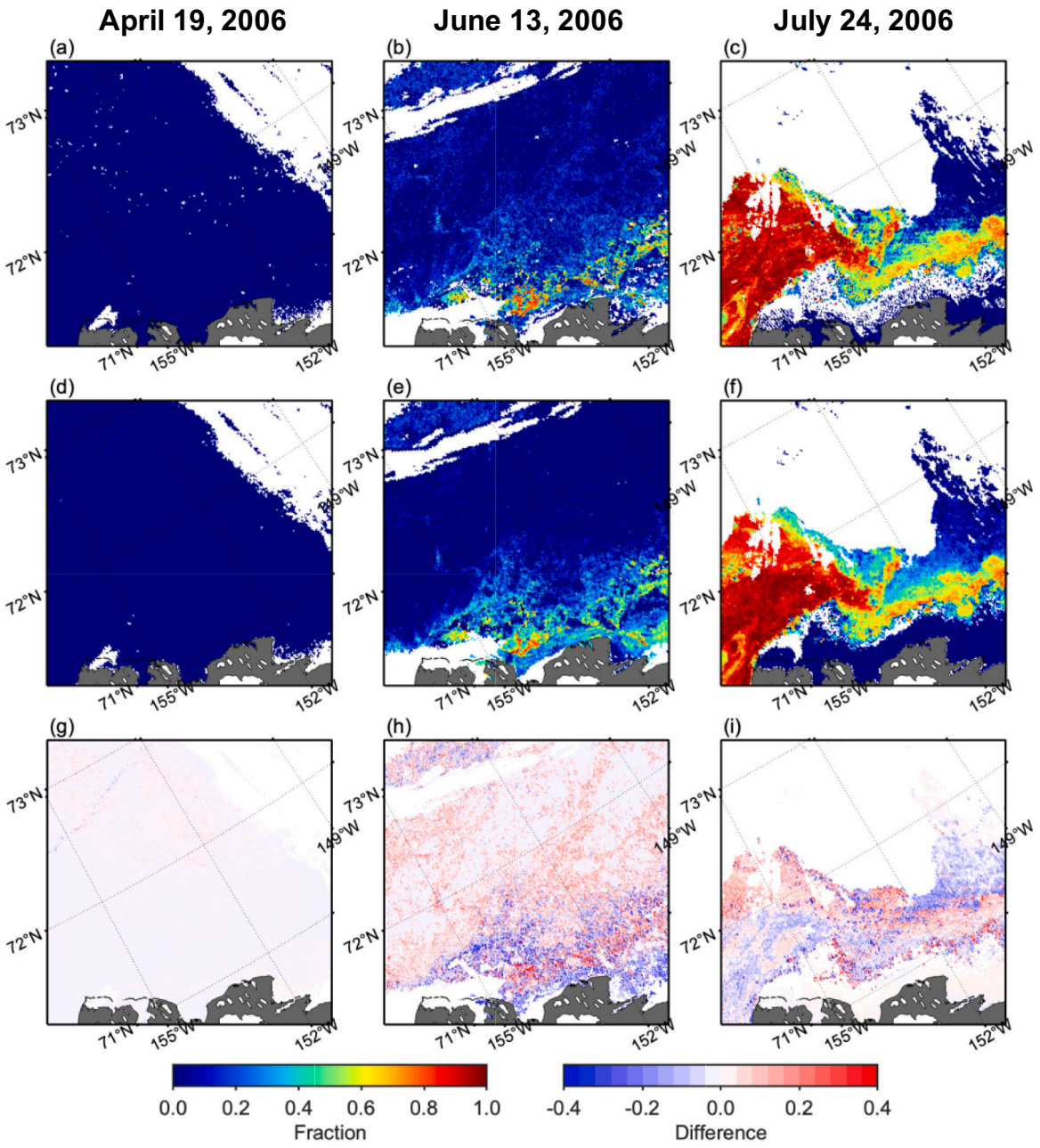

Fig. 10. Spatial patterns in areal fractions of sediment-laden ice retrieved by spectral unmixing algorithms for (a–c) MODIS surface reflectance using only four bands in the visible range, (d–f) MISR surface reflectance, and (g–i) differences in the areal fractions between the two scenes near Point Barrow on April 19, June 13, and July 24, 2006. White pixels were identified as cloud covered by the MODIS cloud mask.

4. Discussion

4.1. Advantages of the proposed approach

This study specified four surface types with two sediment loads for the sediment-laden ice class (50 and 500 g m^{-3}) based on seven MODIS spectral bands. Our sensitivity analyses showed that the proposed approach has sufficient accuracy for estimating areal fraction of not only sediment-laden ice but also other surface types (Tables 1 and 2). Both comparisons of the areal fractions of surface types with true-color images (Figs. 5–8) and spatiotemporal variations in sea ice types (Figs. 12–14) showed reasonable patterns. Comparing with the existing approaches for mapping sediment-laden ice using satellite data (Barber et al., 2021; Huck et al., 2007; Zhang et al., 2015), our approach has the following advantages.

A greater number of spectral bands allows for the capture of spectral variations in surface reflectance through application of a spectral unmixing algorithm. The MODIS sensor has seven spectral bands ranging from the visible to near-infrared range, whereas the MISR sensor has four spectral bands in the visible range (Fig. 4). Our results clearly indicated the superior performance of the spectral unmixing algorithms for MODIS surface reflectance compared to MISR surface reflectance (Tables 1–4). Although spectral differences among surface types were smaller in the near-infrared range than in the visible range (Fig. 4), the many spectral bands with broader spectral coverage would contribute to reducing misclassifications of surface types based on optical properties. As other proposed approaches for detecting sediment-laden ice utilized several MODIS bands (three bands in Barber et al., 2021; and four bands

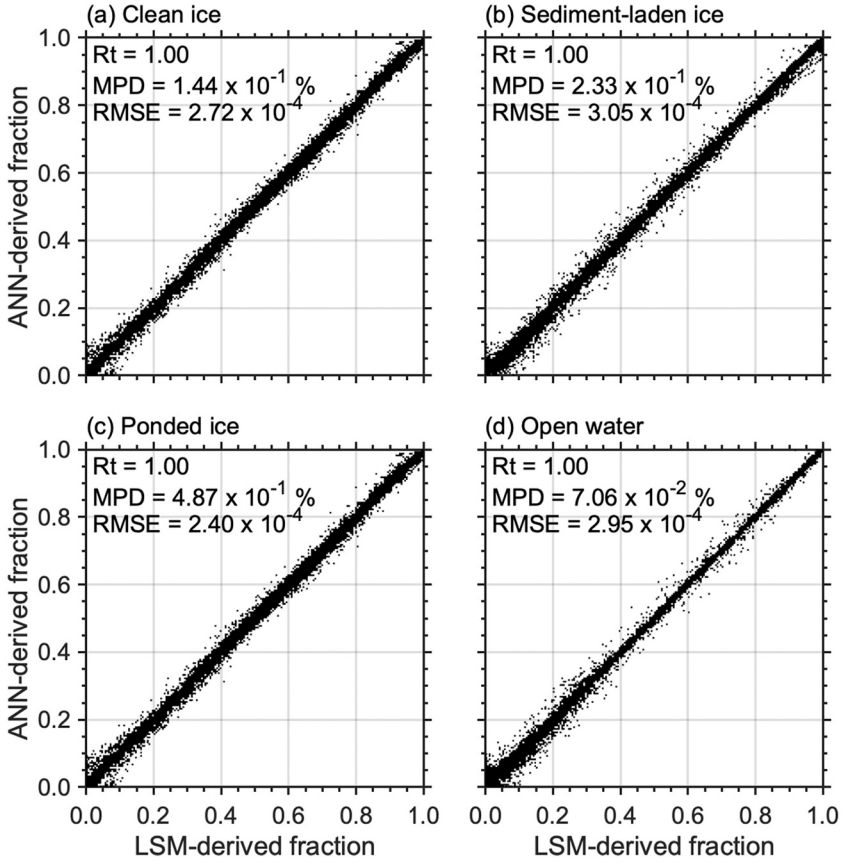

Fig. 11. Scatter plots comparing areal fractions of (a) clean ice, (b) sediment-laden ice, (c) ponded ice, and (d) open water derived from the least square method (LSM) and ANN approach using the MODIS surface reflectance. A total of 2,414,514 (out of 16,096,762) spectra was used for testing the performance of the ANN.

in Zhang et al., 2015) or AVHRR bands (two bands in Huck et al., 2007), our approach has an advantage in the number of spectral bands that can improve the performance of capturing spectral variations.

The proposed approach retrieves areal fractions not only for sediment-laden ice but also other surface types, including clean ice, ponded ice, and open water. The sensitivity analyses demonstrated that the spectral unmixing algorithm for the MODIS surface reflectance retrieves areal fractions of these surface types with estimation error of less than 5% (Table 2). For ponded ice, there are some MODIS and other satellite algorithms for retrieving areal fractions in the Arctic using several bands in the visible range (e.g., four bands in Rösel et al., 2012; three bands in Tschudi et al., 2008). Therefore, the number of spectral bands utilized in the approach taken here represents a strong advantage in the retrieval of both sediment-laden and ponded ice.

Our approach offers areal fractions of sediment-laden ice with more than double the spatial resolution of previously proposed approaches by Huck et al. (2007) and Zhang et al. (2015). Such spatially higher resolution product allows for better discrimination between heterogeneous ice environments and can reduce errors due to a mix of different surface types within a pixel. According to Tucker et al. (1999), sediment concentrations in sea ice measured by their trans-Arctic sampling campaign varied from 2 to 2000 g m^{-3}, and the mean for all samples was 360 g m^{-3} with a standard deviation of 523 g m^{-3}. As sediment-laden ice typically occurs in bands or patches (Eicken et al., 2005; Tucker et al., 1999), spectral signatures of sediment-laden ice would be less prominent at a coarse spatial resolution because other common ice types can overwhelm the sediment-laden ice-specific spectral features. Therefore, our approach with a 500 m spatial resolution would provide a better estimation of sediment-laden ice distribution.

This study constructed an ANN to speed up the processing satellite imagery relative to the spectral unmixing algorithm relying on a least squares method. As the MODIS surface reflectance has a fine spatial resolution of 500 m, processing a time-series of the MODIS surface reflectance at the pan-Arctic scale with a least squares method is a time-consuming process. For a pan-Arctic satellite scene gridded into a polar stereographic projection with 500 m spatial resolution, processing with the ANN was two orders of magnitude faster than with the least squares method. It is important to recall that the resulting areal fractions derived by the ANN showed good agreements with those computed by the least squares method (Fig. 11).

4.2. *Sources of uncertainty and errors*

Arctic sea ice is a complex mosaic of a broader range of surface types (Perovich et al., 2002; Perovich and Polashenski, 2012). Our sensitivity analyses demonstrated the promising performance (Tables 2 and 4) of the approach introduced here to map sediment-laden ice. Nevertheless, several sources of error may require additional work to refine and further enhance the method. Specifically, we utilized spectral albedo as representative of several idealized surface types (Fig. 4) to examine the performance of our approach for a wide variety of hypothetical ice-covered areas and marginal ice zone. For example, spectral albedos for clean ice and sediment-laden ice were simulated as dry surfaces, yet spectral signatures of wet ice surfaces deviate somewhat from those of dry ice surfaces. Wet clean ice causes less incoming solar radiation reflected to space compared to those by dry clean ice (Grenfell and Maykut, 1977), associated with similar shapes of spectral albedo for dry sediment-laden ice with wet clean ice. The analysis indicated that sediment-laden ice accounts for more than 50% of sea ice in late summer and early fall in the Canada Basin (Fig. 12). These values are considered as too high given the deep-water location, distance from the coast and likely ice drift paths (Fig. 2). This is not to exclude the possibility of such

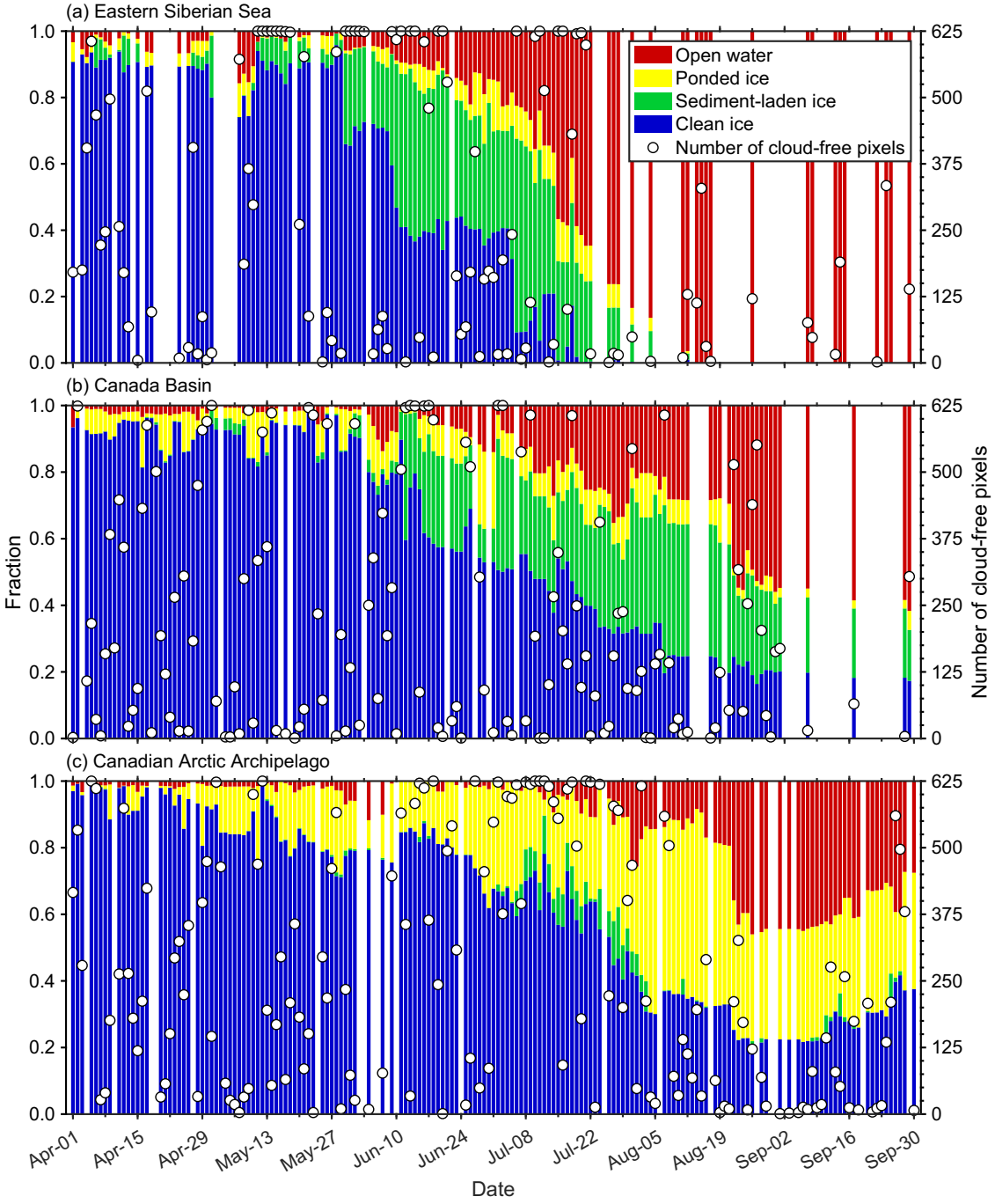

Fig. 12. Seasonal variations in areal fractions of each surface type for 2020 at three sites: (a) East Siberian Sea, (b) Canada Basin, and (c) Canadian Arctic Archipelago. An artificial neural network for estimating areal fractions of each surface type from the MODIS surface reflectance was used to retrieve these fractions. Numbers of cloud-free pixels, depicted as white circles, represent the total cloud-free pixels within the 25 × 25 pixel (12.5 × 12.5 km) subsets for each site (see Fig. 2 for exact locations).

high areal fractions (given that there is good agreement with limited ground truth data for the northern Alaska region (Fig. 1), but without further dedicated ground truthing uncertainty remains. Overall, wet sea ice in summer and fall would be one of the major sources of uncertainty and errors in retrieving the areal fraction of sediment-laden ice, suggesting the sensitivity analyses based on spectral albedo for several idealized surface type may not fully translate into summer conditions for Arctic ice pack settings.

This study assumed that the model-simulated albedo is consistent with the satellite-derived surface reflectance at a single angular position, whereas albedo and surface reflectance are independent, with the satellite-derived reflectances dependent on solar and sensor zenith angles. To resolve and minimize these effects on estimating sediment-laden ice distribution using satellite-derived reflectance data, Huck et al. (2007) generated a look-up table for correcting satellite-derived reflectance based on bidirectional reflectance distribution functions (BRDF). As the BRDF correction enhanced their method substantially (Huck et al., 2007), minimizing the gap between the model-simulated albedo and satellite-derived surface reflectance can help diminish the ensuing uncertainty and errors.

We should also take into account uncertainties associated with subpixel contaminations. The most representative example of subpixel

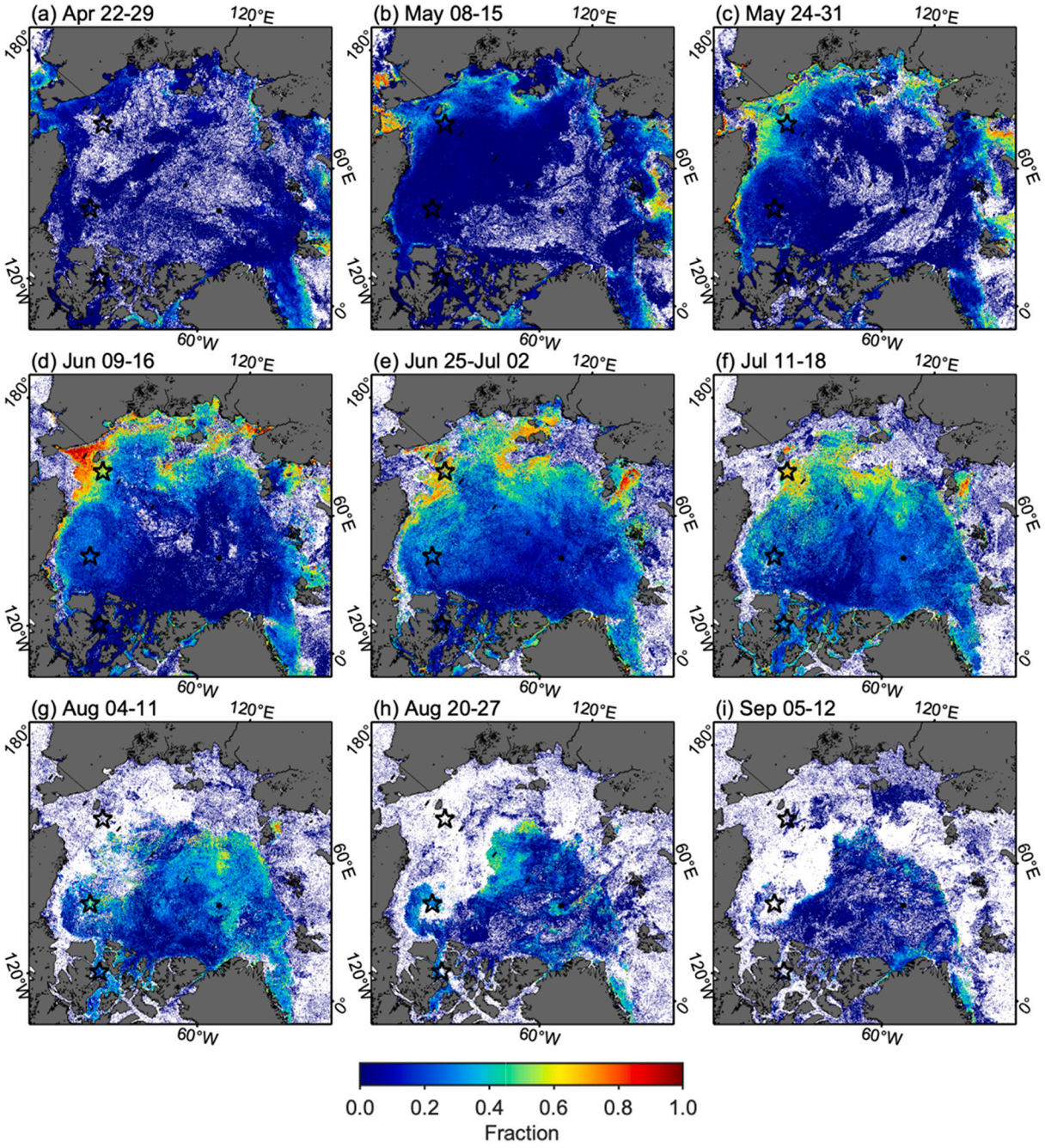

Fig. 13. Every other eight-day averaged areal fractions of sediment-laden ice in the pan-Arctic for 2020. An artificial neural network for estimating areal fractions of each surface type from the MODIS surface reflectance was used to retrieve these fractions. Black stars represent the centers of 25 × 25 pixel (12.5 × 12.5 km) subregions analyzed in the East Siberian Sea, Canada Basin, and Canadian Arctic Archipelago (shown in Fig. 12). White pixels represent the areas where no cloud-free data was available for each eight-day time frame.

contamination would be a substantial non-zero fraction (<0.1) of open water distributed widely in the area at some distance to the coast on April 19, 2006 (Fig. 5e). Excepting sea-ice leads, the ice surface at this time of year would have been covered by snow. One potential explanation for the non-zero fraction of open water aside from visible sea-ice leads (gray lines in Fig. 5a) is that these small values might be associated with subpixel (i.e., <500 m) sea-ice leads which were invisible in the MODIS sensor. Sea-ice leads range from several meters up to several km or even hundreds of km wide, which are more prevalent in areas of thin ice than in the central Arctic ice pack (Wadhams et al., 1985), indicating certain portions of sea-ice leads are likely to be invisible from the MODIS sensor. It is important to note here that the subpixel contamination would not be the only factor producing non-zero fractions of open water before ice melt has commenced. Rather, a complex mixture of all potential factors described in this section could have contributed to producing uncertainties in our results, including the non-zero open water fraction during the snow-covered season.

Another potential source of errors and uncertainties is the MODIS cloud mask that identifies four categories of cloud state (clear, cloud, mixed, and not set - assumed clear) and two categories for cloud shadow (presence and absence). The influence of clouds is a serious problem for measurements of surface reflectance from satellites; however, uncertainties still exist in the MODIS cloud mask which can introduce errors into MOD09 product applications (Liu and Liu, 2013), particularly

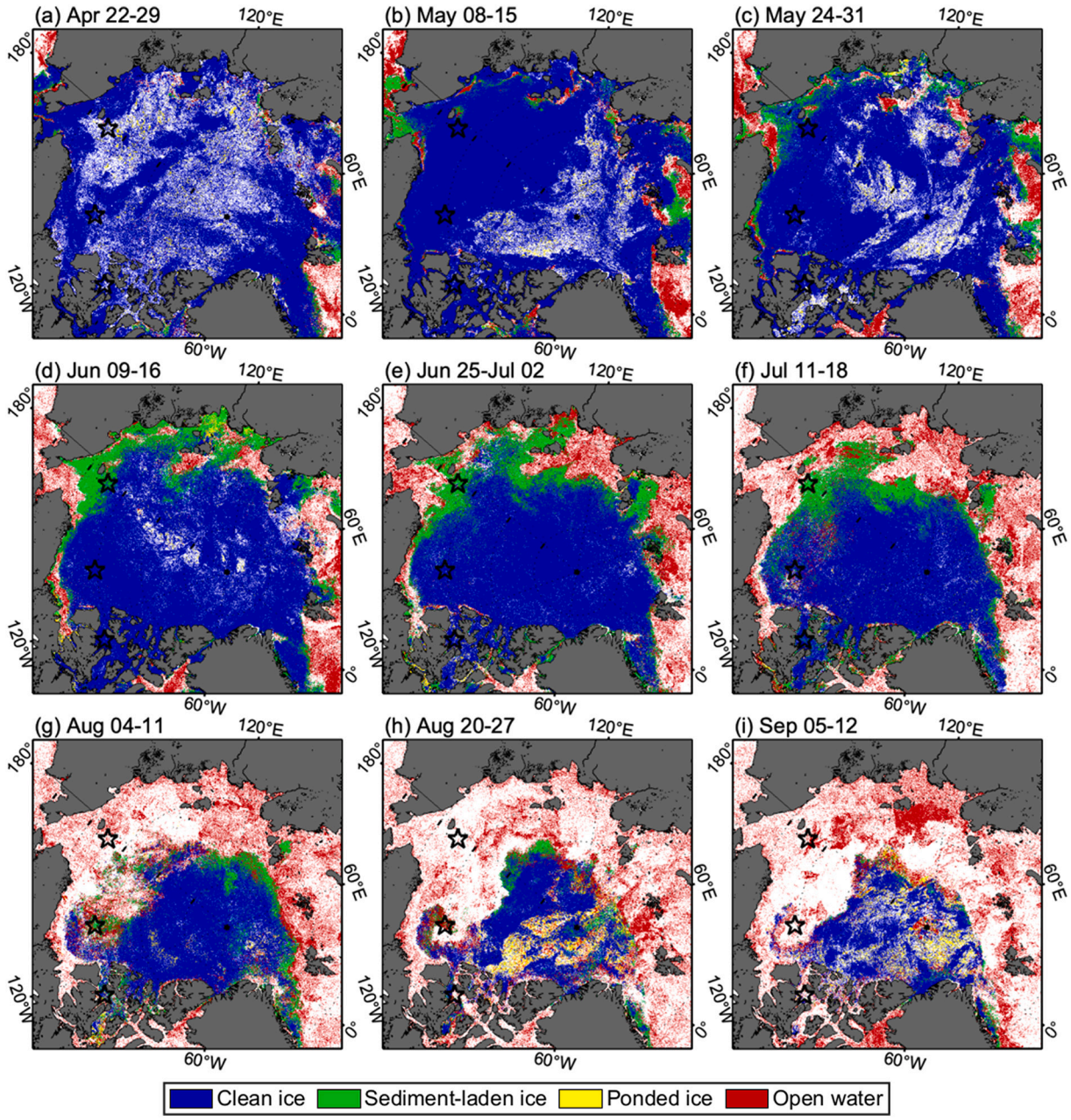

Fig. 14. Spatial distributions of the dominant surface types in the pan-Arctic for 2020. The dominant surface type was determined based on every other eight-day averaged areal fractions of each surface type retrieved by an artificial neural network from the MODIS surface reflectance. Black stars represent the centers of 25 × 25 pixel (12.5 × 12.5 km) subregions analyzed in the East Siberian Sea, Canada Basin, and Canadian Arctic Archipelago (shown in Fig. 12). White pixels represent the areas where no cloud-free data was available for each eight-day time frame.

for the Arctic because the MODIS cloud mask is not tailored towards brighter surfaces comprising snow and ice. Indeed, we found a cloud shadow even after applying the MODIS cloud mask to the MOD09 product (Fig. 6a), resulting in patchy areas with unrealistically high fractions of ponded ice (Fig. 6e) along the cloud shadow. As areal fractions of ponded ice apart from the cloud shadow were consistently small, the patchy area was likely misclassified as ponded ice due to the cloud shadow that should have been masked out by the MODIS cloud mask.

In the Canadian Arctic Archipelago, areal fractions of ponded ice typically show high values shortly after melt ponds begin to form. For example, Li et al. (2020b) examined seasonal variations in melt pond coverage in 2017 based on WorldView-2 satellite images and reported that the ponded ice coverage reached a seasonal maximum of 54% on first-year ice in late June 2017. Similarly, using the MODIS melt pond coverages dataset for 2009–2011 (Rösel et al., 2012), Howell et al. (2020) reported that initial melt pond formation occurred in May with the peak melt pond coverage in early June to mid-July. Overall, we observed a clear difference in the timing of peak ponded ice coverage in the Canadian Arctic Archipelago between the present (mid-August; Fig. 12) and previous studies (Howell et al., 2020; Li et al., 2020b). For the East Siberian Sea and Canada Basin, the areal fraction of ponded ice remained low through April to September compared to previous studies (Fig. 12). One potential factor for this discrepancy is the misclassification of sediment-laden ice as ponded ice in past studies. As spectral albedo of sediment-laden ice is similar to that of ponded ice with high sediment loads particularly in the visible range (Fig. 4), previous studies not accounting for sediment-laden ice would have misclassified

sediment-laden ice as ponded ice. This scenario is particularly relevant for the East Siberian Sea and the Canada Basin with previously described occurrences of sediment-laden ice, whereas it is less likely the origin of differences observed in the Canadian Arctic Archipelago. Without further dedicated validation/calibration procedures, it is not clear whether the aforementioned uncertainties or other unrecognized factors such as interannual variability drove these inconsistencies in ponded ice coverages between the present and previous studies.

4.3. Sediment-laden ice distribution

Seasonal variations in the areal fractions of different surface types showed patterns that conform with results from previous studies (Fig. 12). In the Arctic, the surface snow layer begins to diminish in thickness and extent during the early melt phase giving way to bare ice and ponded ice surfaces (Eicken et al., 2002). While sediment-laden ice was negligible in the early melt phase because sediments are typically distributed throughout the upper ice layers and the ice interior and only begin to be exposed and accumulate at the ice surface once melt has commenced (Eicken et al., 2005; Nürnberg et al., 1994). Indeed, our satellite-based approach retrieved substantial areal fractions of sediment-laden ice in the East Siberian Sea and Canada Basin when ice melt progressed and matured in summer, whereas that of the Canadian Arctic Archipelago was quite small compared with those observed in the East Siberian Sea and Canada Basin – as to be expected for a region with comparatively deep water and fewer records of sediment-laden ice (Fig. 12). It is important to clarify that the proposed approach cannot detect sediments in the interior and lower layers of the ice because of the optically thick surface snow and ice layers (Grenfell, 1983, 1991), indicating large-scale spatial distributions of sediment-laden ice in this study would have not have reflected the actual distribution of sediment-laden ice until after surface snow and clean ice had been removed as a result of melt progression.

Sediment-laden ice was the dominant surface type in coastal areas, particularly in the Siberian, Chukchi, and Beaufort shelves (Fig. 14). These regional patterns in sediment-laden ice correspond with those in previous studies reporting sediment inclusions are often associated with entrainment of frazil ice into deformed, multiple layers of rafted nilas, indicative of a flaw-lead environment adjacent to the landfast ice of the Chukchi and Beaufort shelves (Eicken et al., 2005; Tucker et al., 1999). Note also that satellite data show a high incidence of sediment-laden ice in the East Siberian and Laptev Seas surrounding the New Siberian Islands, which conforms with previous findings that pointed to this region as a major source area of sediments (Eicken et al., 2000), fostered also by high tidal current velocities in this region (Baumann et al., 2020; Lyard, 1997). In consequence, we confirmed the spatial distribution of sediment-laden ice retrieved from satellite data were broadly consistent with previous findings based on in situ measurements.

In addition, we also identified substantial areal fractions of sediment-laden ice in the central Arctic (Fig. 13). As sediment entrainment into sea ice would not occur over deep waters at quite some distance to the coast (Ito et al., 2015, 2019), it is anticipated that sediment-laden ice observed in the central Arctic would have been transported from coastal areas. In fact, Krumpen et al. (2020) reported that the ice formed around the New Siberian Islands in winter with inclusions of sediment was transported to the central Arctic Ocean. Therefore, major Arctic coastal polynyas over shallow continental shelves, such as the East Siberian Sea and Chukchi Sea coastal polynyas (Tamura and Ohshima, 2011), and potentially broken-out landfast ice (Eicken et al., 2005; Tucker et al., 1999) are likely to be primary sources of sediment-laden ice not only in coastal areas but also in the central Arctic.

4.4. Implications for future work

As shown in the comparison result in the spectral unmixing algorithms between the MODIS and MISR surface reflectance (Figs. 9–10), higher spectral resolution can improve capture of spectral variations associated with ice surface heterogeneity. In addition, with more spectral bands, more surface types can be specified in the spectral unmixing algorithm. Thus, the accuracy of estimating areal fractions of surface types would improve by using advanced multispectral and hyperspectral satellite sensors employed in the future. An alternative approach for improving retrieval accuracy with the existing multispectral satellite sensors is to utilize spectral band ratios which can highlight differences in spectral signature between the two bands. Lee et al. (2020) developed a satellite capability to detect melt ponds on Arctic sea ice using various combinations of band ratios in MODIS surface reflectance. Although the spectral unmixing algorithm would not be directly applicable to the band ratio method, there is a potential to retrieve areal fractions of each surface type accurately.

One of the most important steps in future work is to confirm the robustness of the proposed approach by validating and calibrating the performance using actual in situ data. Although our results presented in this study showed reasonable consistency with previously established field-based findings, a quantitative assessment of the performance was beyond the scope of this study. As errors in satellite products are known unknowns, quantifying their uncertainties by analytical comparison with actual data is a crucial requirement from the end user perspective (Loew et al., 2017; Otto et al., 2016). While our sensitivity analyses demonstrated accurate performance of the proposed approach for a wide range of hypothetical ice surfaces, we identified several sources of uncertainty and errors as detailed in section 4.2. Therefore, field-based validation and calibration procedures are required to identify time periods (e.g., melting and freezing seasons), ice surface and cloud conditions, and geographical areas for which sediment-laden ice can be mapped reliably. Such dedicated future work would provide convincing evidence that the technique can be a powerful tool across different research fields.

Sediments incorporated into sea ice act as an important source of iron and nutrients (Kanna et al., 2014; Nomura et al., 2010), which support phytoplankton population growth and, in turn, the development of phytoplankton blooms in spring. Conversely, turbid meltwater released from sediment-laden ice suppresses growth of phytoplankton because turbid meltwater drastically decreases light penetration into the water column (Nishioka et al., 2014). These two conflicting impacts of sediment-laden ice could likely affect spring phytoplankton bloom dynamics, particularly the timing of spring phytoplankton blooms that is a crucial factor for Arctic marine ecosystems (Campbell et al., 2009; Grebmeier and McRoy, 1989). Besides, sea-ice transport of sediments plays an important role in the redistribution and dispersal of pollutants (Pfirman et al., 1995) originating from coastal and inland sources such as river flows, coastal erosion, and oil and gas exploration and development (Kasper et al., 2017). Moreover, discrimination of clean and sediment-laden ice based on our approach contributes to more accurate estimates of solar heating in the Arctic, because sediment-laden ice has a substantially lower albedo than clean ice (Fig. 4). Thus, a near real-time and cost-effective satellite-based approach for monitoring spatiotemporal variations in the distribution of sediment-laden ice could be an effective tool for a wide variety of research fields.

5. Summary and conclusions

This study introduced a near real-time and efficient satellite-based approach for the detection and mapping of sediment-laden ice. As the spectral characteristics of sediment-laden ice differ from those other surface types, the fraction of sediment-laden ice was estimated from the remotely-sensed surface reflectance based on a spectral unmixing algorithm. Although our approach contains potential uncertainties associated with methodological limitations, spatiotemporal variations in sediment-laden ice exhibited reasonable agreement with spatial patterns and seasonal variations reported in the literature that reported in situ observations of sediment-laden ice. As the role of sediment-laden ice

in biogeochemical cycling is very different from that of clean ice but still poorly understood, satellite-based monitoring of sediment-laden ice along with in situ observations and model simulations can foster our understanding of the impacts of sediment-laden ice on a wide variety of research fields including sediment transport and biogeochemical cycling.

Declaration of Competing Interest

The authors declare that they have no known competing financial interests or personal relationships that could have appeared to influence the work reported in this paper.

Acknowledgements

The MISR BHR data was produced and distributed by the Quality Assurance for Essential Climate Variables (QA4ECV) project (http://www.qa4ecv.eu/) of the European Union's Seventh Framework Programme. The ocean color data were produced and distributed by the Distributed Active Archive Center at the Goddard Space Flight Center. Sea-ice concentration data were provided by the National Snow and Ice Data Center at the University of Colorado. This work was supported by the Ministry of Education, Culture, Sports, Science, and Technology of Japan (MEXT) through the Arctic Challenge for Sustainability II (ArCS II), and the Grant-in-Aids for JSPS Overseas Research Fellowships, Early-Career Scientists 21K14894, and Scientific Research (B) 19H01961. This work was also supported by the Arctic Challenges for Sustainability (ArCS) Program for Overseas Visit by Young Researchers. This research was partly funded by the Interdisciplinary Research for Arctic Coastal Environments (InteRFACE) project through the U.S. Department of Energy, Office of Science, Biological and Environmental Research RGMA program. BL gratefully acknowledges support from NSF Office of Polar Programs grant OPP-1724467.

References

Atkinson, P.M., Tatnall, A.R.L., 1997. Introduction neural networks in remote sensing. Int. J. Remote Sens. https://doi.org/10.1080/014311697218700.

Barber, D.G., Harasyn, M.L., Babb, D.G., Capelle, D., McCullough, G., Dalman, L.A., Matthes, L.C., Ehn, J.K., Kirillov, S., Kuzyk, Z., Basu, A., Fayak, M., Schembri, S., Papkyriakou, T., Ahmed, M.M.M., Else, B., Guéguen, C., Meilleur, C., Dmitrenko, I., Mundy, C.J., Gupta, K., Rysgaard, S., Stroeve, J., Sydor, K., 2021. Sediment-laden sea ice in southern Hudson Bay: entrainment, transport, and biogeochemical implications. Elem. Sci. Anth. 9 https://doi.org/10.1525/elementa.2020.00108.

Baumann, T.M., Polyakov, I.V., Padman, L., Danielson, S., Fer, I., Janout, M., Williams, W., Pnyushkov, A.V., 2020. Arctic tidal current atlas. Sci. Data 7, 275. https://doi.org/10.1038/s41597-020-00578-z.

Boulze, H., Korosov, A., Brajard, J., 2020. Classification of sea ice types in Sentinel-1 SAR data using convolutional neural networks. Remote Sens. 12, 2165. https://doi.org/10.3390/rs12132165.

Campbell, R.G., Sherr, E.B., Ashjian, C.J., Plourde, S., Sherr, B.F., Hill, V., Stockwell, D. A., 2009. Mesozooplankton prey preference and grazing impact in the western Arctic Ocean. Deep-Sea Res. II 56, 1274–1289. https://doi.org/10.1016/j.dsr2.2008.10.027.

Chen, N., Li, W., Gatebe, C., Tanikawa, T., Hori, M., Shimada, R., Aoki, T., Stamnes, K., 2018. New neural network cloud mask algorithm based on radiative transfer simulations. Remote Sens. Environ. 219, 62–71. https://doi.org/10.1016/j.rse.2018.09.029.

Darby, D.A., Myers, W.B., Jakobsson, M., Rigor, I., 2011. Modern dirty sea ice characteristics and sources: the role of anchor ice. J. Geophys. Res. Atmos. 116 https://doi.org/10.1029/2010JC006675.

Eicken, H., Kolatschek, J., Freitag, J., Lindemann, F., Kassens, H., Dmitrenko, I., 2000. A key source area and constraints on entrainment for basin-scale sediment transport by Arctic sea ice. Geophys. Res. Lett. 27, 1919–1922. https://doi.org/10.1029/1999GL011132.

Eicken, H., Krouse, H.R., Kadko, D.C., Perovich, D.K., 2002. Tracer studies of pathways and rates of meltwater transport through Arctic summer sea ice. J. Geophys. Res. 107 (22), 407. https://doi.org/10.1029/2000JC000583.

Eicken, H., Gradinger, R., Gaylord, A., Mahoney, A., Rigor, I., Melling, H., 2005. Sediment transport by sea ice in the Chukchi and Beaufort Seas: increasing importance due to changing ice conditions? Deep-Sea Res. II 52, 3281–3302. https://doi.org/10.1016/j.dsr2.2005.10.006.

Fourrier, M., Coppola, L., Claustre, H., d'Ortenzio, F., Sauzède, R., Gattuso, J.-P., 2020. A regional neural network approach to estimate water-column nutrient concentrations and carbonate system variables in the Mediterranean Sea: CANYON-MED. Front. Mar. Sci. 7, 69. https://doi.org/10.3389/fmars.2020.00620.

Gradinger, R.R., Kaufman, M.R., Bluhm, B.A., 2009. Pivotal role of sea ice sediments in the seasonal development of near-shore Arctic fast ice biota. Mar. Ecol. Prog. Ser. 394, 49–63. https://doi.org/10.3354/meps08320.

Grebmeier, J.M., McRoy, C.P., 1989. Pelagic-benthic coupling on the shelf of the northern Bering and Chukchi Seas. Ill Benthic food supply and carbon cycling. Mar. Ecol. Prog. Ser. 53, 79–91. https://doi.org/10.3354/meps053079.

Grenfell, T.C., 1983. A theoretical model of the optical properties of sea ice in the visible and near infrared. J. Geophys. Res. Oceans 88, 9723–9735. https://doi.org/10.1029/jc088ic14p09723.

Grenfell, T.C., 1991. A radiative transfer model for sea ice with vertical structure variations. J. Geophys. Res. 96, 16991–17001. https://doi.org/10.1029/91JC01595.

Grenfell, T.C., Maykut, G.A., 1977. The optical properties of ice and snow in the Arctic Basin. J. Glaciol. 18, 445–463. https://doi.org/10.3189/s0022143000021122.

Howell, S.E.L., Scharien, R.K., Landy, J., Brady, M., 2020. Spring melt pond fraction in the Canadian Arctic Archipelago predicted from RADARSAT-2. Cryosphere 14, 4675–4686. https://doi.org/10.5194/tc-14-4675-2020.

Hu, S., Liu, H., Zhao, W., Shi, T., Hu, Z., Li, Q., Wu, G., 2018. Comparison of machine learning techniques in inferring phytoplankton size classes. Remote Sens. 10, 191. https://doi.org/10.3390/rs10030191.

Huck, P., Light, B., Eicken, H., Haller, M., 2007. Mapping sediment-laden sea ice in the Arctic using AVHRR remote-sensing data: atmospheric correction and determination of reflectances as a function of ice type and sediment load. Remote Sens. Environ. 107, 484–495. https://doi.org/10.1016/j.rse.2006.10.002.

Ito, M., Ohshima, K.I., Fukamachi, Y., Simizu, D., Iwamoto, K., Matsumura, Y., Mahoney, A.R., Eicken, H., 2015. Observations of supercooled water and frazil ice formation in an Arctic coastal polynya from moorings and satellite imagery. Ann. Glaciol. 56, 307–314. https://doi.org/10.3189/2015AoG69A839.

Ito, M., Ohshima, K.I., Fukamachi, Y., Hirano, D., Mahoney, A.R., Jones, J., Takatsuka, T., Eicken, H., 2019. Favorable conditions for suspension freezing in an Arctic coastal polynya. J. Geophys. Res. Oceans 266, 261. https://doi.org/10.1029/2019JC015536.

Kanna, N., Toyota, T., Nishioka, J., 2014. Iron and macro-nutrient concentrations in sea ice and their impact on the nutritional status of surface waters in the southern Okhotsk Sea. Prog. Oceanogr. 126, 44–57. https://doi.org/10.1016/j.pocean.2014.04.012.

Kasper, J., Dunton, J.H., Schonberg, S.V., Trefry, J., Bluhm, B., Durell, G.S., 2017. Arctic Nearshore Impact Monitoring in Development Area (ANIMIDA) III: Contaminants, Sources, and Bioaccumulation. U.S. Dept. of the Interior, Bureau of Ocean Energy Management, Alaska OCS Region, Anchorage, AK.

Kharbouche, S., Muller, J.-P., 2019. Sea ice albedo from MISR and MODIS: production, validation, and trend analysis. Remote Sens. 11, 9. https://doi.org/10.3390/rs11010009.

Krumpen, T., Birrien, F., Kauker, F., Rackow, T., von Albedyll, L., Angelopoulos, M., Belter, H.J., Bessonov, V., Damm, E., Dethloff, K., Haapala, J., Haas, C., Harris, C., Hendricks, S., Hoelemann, J., Hoppmann, M., Kaleschke, L., Karcher, M., Kolabutin, N., Lei, R., Lenz, J., Morgenstern, A., Nicolaus, M., Nixdorf, U., Petrovsky, T., Rabe, B., Rabenstein, L., Rex, M., Ricker, R., Rohde, J., Shimanchuk, E., Singha, S., Smolyanitsky, V., Sokolov, V., Stanton, T., Timofeeva, A., Tsamados, M., Watkins, D., 2020. The MOSAiC ice floe: sediment-laden survivor from the Siberian shelf. Cryosphere 14, 2173–2187. https://doi.org/10.5194/tc-14-2173-2020.

Kulp, S.A., Strauss, B.H., 2018. CoastalDEM: a global coastal digital elevation model improved from SRTM using a neural network. Remote Sens. Environ. 206, 231–239. https://doi.org/10.1016/j.rse.2017.12.026.

Lee, S., Stroeve, J., Tsamados, M., Khan, A.L., 2020. Machine learning approaches to retrieve pan-Arctic melt ponds from visible satellite imagery. Remote Sens. Environ. 247, 111919 https://doi.org/10.1016/j.rse.2020.111919.

Lei, R., Zhang, Z., Matero, I., Cheng, B., Li, Q., Huang, W., 2012. Reflection and transmission of irradiance by snow and sea ice in the central Arctic Ocean in summer 2010. Polar Res. 31, 17325. https://doi.org/10.3402/polar.v31i0.17325.

Li, X., Bellerby, R.G.J., Wallhead, P., Ge, J., Liu, J., Liu, J., Yang, A., 2020a. A neural network-based analysis of the seasonal variability of surface total alkalinity on the East China Sea shelf. Front. Mar. Sci. 7 https://doi.org/10.3389/fmars.2020.00219.

Li, Q., Zhou, C., Zheng, L., Liu, T., Yang, X., 2020b. Monitoring evolution of melt ponds on first-year and multiyear sea ice in the Canadian Arctic Archipelago with optical satellite data. Ann. Glaciol. 61, 154–163. https://doi.org/10.1017/aog.2020.24.

Light, B., Eicken, H., Maykut, G.A., Grenfell, T.C., 1998. The effect of included participates on the spectral albedo of sea ice. J. Geophys. Res. 103, 27739–27752. https://doi.org/10.1029/98JC02587.

Liu, R., Liu, Y., 2013. Generation of new cloud masks from MODIS land surface reflectance products. Remote Sens. Environ. 133, 21–37. https://doi.org/10.1016/j.rse.2013.01.019.

Loew, A., Bell, W., Brocca, L., Bulgin, C.E., Burdanowitz, J., Calbet, X., Donner, R.V., Ghent, D., Gruber, A., Kaminski, T., Kinzel, J., Klepp, C., Lambert, J., Schaepman-Strub, G., Schröder, M., Verhoelst, T., 2017. Validation practices for satellite-based Earth observation data across communities. Rev. Geophys. 55, 779–817. https://doi.org/10.1002/2017rg000562.

Lyard, F.H., 1997. The tides in the Arctic Ocean from a finite element model. J. Geophys. Res. 102, 15611–15638. https://doi.org/10.1029/96jc02596.

Marzban, C., 2009. Artificial Intelligence Methods in the Environmental Sciences. Springer Netherlands, Dordrecht. https://doi.org/10.1007/978-1-4020-9119-3.

Mélin, F., Vantrepotte, V., 2015. How optically diverse is the coastal ocean? Remote Sens. Environ. 160, 235–251. https://doi.org/10.1016/j.rse.2015.01.023.

Nishioka, J., Mitsudera, H., Yasuda, I., Liu, H., Nakatsuka, T., Volkov, Y.N., 2014. Biogeochemical and physical processes in the Sea of Okhotsk and the linkage to the Pacific. Prog. Oceanogr. 126, 1–7. https://doi.org/10.1016/j.pocean.2014.04.027.

Nomura, D., Nishioka, J., Granskog, M.A., Krell, A., Matoba, S., Toyota, T., Hattori, H., Shirasawa, K., 2010. Nutrient distributions associated with snow and sediment-laden layers in sea ice of the southern Sea of Okhotsk. Mar. Chem. 119, 1–8. https://doi.org/10.1016/j.marchem.2009.11.005.

Nürnberg, D., Wollenburg, I., Dethleff, D., Eicken, H., Kassens, H., Letzig, T., Reimnitz, E., Thiede, J., 1994. Sediments in Arctic sea ice: implications for entrainment, transport and release. Mar. Geol. 119, 185–214. https://doi.org/10.1016/0025-3227(94)90181-3.

Otto, J., Brown, C., Buontempo, C., Doblas-Reyes, F., Jacob, D., Juckes, M., Keup-Thiel, E., Kurnik, B., Schulz, J., Taylor, A., Verhoelst, T., Walton, P., 2016. Uncertainty: lessons learned for climate services. Bull. Am. Meteor. Soc. 97 https://doi.org/10.1175/bams-d-16-0173.1. ES265–ES269.

Paul, S., Huntemann, M., 2021. Improved machine-learning-based open-water–sea-ice–cloud discrimination over wintertime Antarctic sea ice using MODIS thermal-infrared imagery. Cryosphere 15, 1551–1565. https://doi.org/10.5194/tc-15-1551-2021.

Pegau, W.S., Paulson, C.A., 2001. The albedo of Arctic leads in summer. Ann. Glaciol. 33, 221–224. https://doi.org/10.3189/172756401781818833.

Perovich, D.K., Polashenski, C., 2012. Albedo evolution of seasonal Arctic sea ice. Geophys. Res. Lett. 39 https://doi.org/10.1029/2012GL051432 n/a–n/a.

Perovich, D.K., Grenfell, T.C., Light, B., Hobbs, P.V., 2002. Seasonal evolution of the albedo of multiyear Arctic sea ice. J. Geophys. Res. 107 (12) https://doi.org/10.1029/2000JC000438, 417–13.

Perovich, D.K., Grenfell, T.C., Richter-Menge, J.A., Light, B., Tucker, W.B., Eicken, H., 2003. Thin and thinner: sea ice mass balance measurements during SHEBA. J. Geophys. Res. Oceans 108 (C3), 8050. https://doi.org/10.1029/2001jc001079.

Perovich, D.K., Light, B., Eicken, H., Jones, K.F., Runciman, K., Nghiem, S.V., 2007. Increasing solar heating of the Arctic Ocean and adjacent seas, 1979–2005: attribution and role in the ice-albedo feedback. Geophys. Res. Lett. 34, L19505. https://doi.org/10.1029/2007GL031480.

Perovich, D., Polashenski, C., Arntsen, A., Stwertka, C., 2017. Anatomy of a late spring snowfall on sea ice. Geophys. Res. Lett. 44, 2802–2809. https://doi.org/10.1002/2016gl071470.

Pfirman, S.L., Eicken, H., Bauch, D., Weeks, W.F., 1995. The potential transport of pollutants by Arctic sea ice. Sci. Total Environ. 159, 129–146. https://doi.org/10.1016/0048-9697(95)04174-Y.

Robilliard, D., Fonlupt, C., 2002. Backwarding: An overfitting control for genetic programming in a remote sensing application. In: Collet, P., Fonlupt, C., Hao, J.K., Lutton, E., Schoenauer, M. (Eds.), Artificial Evolution. Springer, Heidelberg, pp. 245–254. https://doi.org/10.1007/3-540-46033-0_20.

Rösel, A., Kaleschke, L., Birnbaum, G., 2012. Melt ponds on Arctic sea ice determined from MODIS satellite data using an artificial neural network. Cryosphere 6, 431–446. https://doi.org/10.5194/tc-6-431-2012.

Rumelhart, D.E., Hinton, G.E., Williams, R.J., 1986. Learning representations by back-propagating errors. Nature 323, 533–536.

Sauzède, R., Claustre, H., Uitz, J., Jamet, C., Dall'Olmo, G., D'Ortenzio, F., Gentili, B., Poteau, A., Schmechtig, C., 2016. A neural network-based method for merging ocean color and Argo data to extend surface bio-optical properties to depth: retrieval of the particulate backscattering coefficient. J. Geophys. Res. Oceans 121, 2552–2571. https://doi.org/10.1002/2015JC011408.

Shah, C.A., Varshney, P.K., 2004. A higher order statistical approach to spectral unmixing of remote sensing imagery. IEEE Int. Geosci. Remote Sens. Sympos. 2, 1065–1068. https://doi.org/10.1109/igarss.2004.1368595.

Syariz, M.A., Lin, C.-H., Van Nguyen, M., Jaelani, L.M., Blanco, A.C., 2020. WaterNet: a convolutional neural network for chlorophyll-a concentration retrieval. Remote Sens. 12, 1966. https://doi.org/10.3390/rs12121966.

Tamura, T., Ohshima, K.I., 2011. Mapping of sea ice production in the Arctic coastal polynyas. J. Geophys. Res. 116, 529. https://doi.org/10.1029/2010JC006586.

Tschudi, M.A., Maslanik, J.A., Perovich, D.K., 2008. Derivation of melt pond coverage on Arctic sea ice using MODIS observations. Remote Sens. Environ. 112, 2605–2614. https://doi.org/10.1016/j.rse.2007.12.009.

Tucker, W.B., Gow, A.J., Meese, D.A., Bosworth, H.W., Reimnitz, E., 1999. Physical characteristics of summer sea ice across the Arctic Ocean. J. Geophys. Res. Atmos. 104, 1489–1504. https://doi.org/10.1029/98JC02607.

Wadhams, P., McLaren, A.S., Weintraub, R., 1985. Ice thickness distribution in Davis Strait in February from submarine sonar profiles. J. Geophys. Res. Oceans 90, 1069–1077. https://doi.org/10.1029/jc090ic01p01069.

Zhang, D., Ke, C., Sun, B., Lei, R., Tang, X., 2011. Extraction of sea ice concentration based on spectral unmixing method. J. Appl. Remote. Sens. 5 https://doi.org/10.1117/1.3643703, 053552-053552–10.

Zhang, N., Wu, Y., Zhang, Q., 2015. Detection of sea ice in sediment laden water using MODIS in the Bohai Sea: a CART decision tree method. Int. J. Remote Sens. 36, 1661–1674. https://doi.org/10.1080/01431161.2015.1015658.